

THESIS FOR THE DEGREE OF DOCTOR OF PHILOSOPHY

**Characterization of nano-scale materials for interconnect
and thermal dissipation application in electronics packaging**

Xin Luo



CHALMERS

Department of Microtechnology and Nanoscience (MC2)

BioNano Systems Laboratory

CHALMERS UNIVERSITY OF TECHNOLOGY

Göteborg, Sweden 2014

Characterization of nano-scale materials for interconnect and thermal dissipation application in electronics packaging

Xin Luo

Göteborg, August 2014

© Xin Luo, 2014

ISBN 978-91-7597-046-2

Doktorsavhandlingar vid Chalmers tekniska Högskola

Ny serie nr 3727

ISSN 0346-718X

Technical Report MC2-279

ISSN 1652-0769

Bio-Nano System Laboratory

Department of Microtechnology and Nanoscience (MC2)

Chalmers University of Technology

SE-412 96 Göteborg, Sweden

Phone: +46 (0)31 772 1000

Printed by Chalmers Reproservice

Göteborg, Sweden 2014

Characterization of nano-scale materials for interconnect and thermal dissipation application in electronics packaging

Xin Luo

Department of Microtechnology and Nanoscience

Chalmers University of Technology

Abstract

This thesis focuses on studies of nano-scale materials in electronic packaging applications with respect to following aspects: surface analysis of nano-scale oxide of lead-free solder particles, and thermal performance and mechanical property studies of nano-scale fiber and metal composite-based thermal interface materials.

The composition and thickness of the solder oxide have a direct impact on the quality of interconnects and the reliability of a packaged system. The characterization of the nano-scale oxide of lead-free solder particles is investigated by transmission electron microscopy and scanning transmission electron microscopy. The solder powders are exposed to air at 150 °C for 0, 120 and 240 h. The oxide thickness is 6 nm and 50 nm measured by STEM for 0 h and 120 h samples, respectively. The increase in oxide thickness of solder particles is proportional to the rooting of the oxidation time. The intersection analysis method for analyzing Auger electron spectroscopy depth profiles is also presented which could be expand to analyze oxide of other alloy, i.e. Cu, Ag or stainless steel.

In the next part of this thesis, a new composite design consisting of electrospun polyimide fiber networks and infiltrated metal matrix is presented. Three composites are fabricated including polyimide fiber-InSnBi, polyimide fiber-indium and polyimide fiber-SnAgCu composites. The microstructure of the composite is investigated by scanning electron microscopy, energy dispersive X-ray detector and X-ray diffraction, showing a good bonding between the fibers and the metal matrix. These composites demonstrate high thermal conductivity, low thermal contact resistance and reliable thermomechanical performance during thermal cycling. The polyimide fiber-indium composites are sandwiched between chips and heat spreaders with different packaged sizes to detect the junction temperature and junction-to-case thermal resistance. The shear strength of the polyimide fiber-indium composite between Sn surfaces can reach 4 MPa which is larger than that with Au and Cu surfaces. Both composites present good reliability during the humidity-heat aging tests. The polyimide fiber-indium composite's ultimate tensile strength at 20 °C is five times higher than that of the pure indium, and the tensile strength of the composite exceeds the summation of those from its individual components. With the increase in temperature, the ultimate tensile strength declines but still precedes pure indium and the elongation at fracture increases. Contrary to most metallic materials, the ultimate tensile strength of the composite is inversely proportional to the logarithmic strain rate in a certain range. Finally, a new strengthening mechanism is presented based on mutually reinforcing structures formed by the indium and surrounding fibers, underlining the effect of compressing at the fiber-indium interfaces by dislocation pileups and slip pinning. The creep threshold of the composite corresponds to the

fracture strength of the polyimide fiber, and the step-like sudden increases of the composite's creep strain are due to the breakage of fibers. The fiber-indium interfaces are also beneficial to the composite's creep resistance. In the final part of the thesis, two novel thermal interface materials are developed and characterized including boron nitride fiber-indium composite and carbon fiber-SnAgCu composite. Thermally conductive boron nitride fiber or carbon fiber is prepared via electrospinning and heat treatment. Afterward, the boron nitride/carbon fibers are sputtered with Ti/Au coatings and infiltrated with metal matrix. Good in-plane and through-plane thermal conductivity of the thermally conductive fiber-metal matrix composite are obtained using a laser flash apparatus.

Keywords: lead-free solder, nano-scale oxide layer, electrospun nanofiber, metal matrix composite, thermal interface material, thermal conductivity, thermal management, boron nitride fiber, carbon fiber.

To my wife Lulu Shi and our parents. Their love fully warms my heart and none thermal interface material could dissipate the heat.

List of publications

Appended papers

This thesis is based on the following appended papers:

A Surface oxide analysis of lead-free solder particles

Xin, Luo; Wenhui, Du; Xiuzhen, Lu; Toshikazu, Yamaguchi; Jackson, Gavin; Lilei, Ye; Johan, Liu
Soldering & Surface Mount Technology, 2013, 25(1), pp. 39 - 44

B Unusual tensile behaviour of fiber-reinforced indium matrix composite and its in-situ TEM straining observation

Xin, Luo; Jianchao, Peng; Carl, Zandén; Yanping, Yang; Wei, Mu; Lilei, Ye; Johan, Liu
Submitted to Acta Materialia

C High creep resistance of polyimide fiber-reinforced indium matrix composite and its in-situ TEM straining analysis

Xin, Luo; Wei, Mu; Carl, Zandén; Lilei, Ye; Jianchao, Peng; Johan, Liu
Submitted to Applied Physics Letter

D Study on the heat dissipation mechanism and mechanical performance of metal-based nano thermal interface material in electronic packaging

Shuangxi, Sun; **Xin, Luo**; Si, Chen; Carl, Zandén; Lilei, Ye; Johan, Liu
Minor revision changed required, revised version submitted to IEEE CPMT Transactions

E Study on the reliability of nano-structured polymer-metal composite for thermal interface material

Lei, Zhang; **Xin, Luo**; Xiuzhen, Lu; Johan, Liu
Electro Chemical Society (ECS) Transactions, 2011, 34 (1) pp. 991- 995.

F A new solder matrix nano polymer composite for thermal management applications

Carl, Zandén; **Xin, Luo**; Lilei, Ye; Johan, Liu
Composites Science and Technology, 2014, 94(0) pp. 54-61.

G Novel thermal interface materials: boron nitride nanofiber and indium composites for electronics heat dissipation applications.

Xin, Luo; Yong, Zhang; Carl, Zandén; Murali, Murugesan; Yu, Cao; Lilei, Ye; Johan, Liu
Journal of Materials Science: Materials in Electronics, 2014, 25(5) pp. 2333-2338

H Carbon fiber solder matrix composite for thermal management of high power electronics

Murali, Murugesan; Carl, Zandén; **Xin, Luo**; Lilei, Ye; Valdas, Jokubavicius; Mikael, Syväjärvi; Johan, Liu

Accepted by Journal of Materials Chemistry C

Other contributions

Other papers not included in the thesis:

A Characterization of surface oxide of lead-free solder particle by TEM and STEM

Xin, Luo; Wenhui, Du; Xiuzhen, Lu; Toshikazu, Yamaguchi; Jackson, Gavin; Lilei, Ye; Eehua, Wong; Johan, Liu
International Conference on Electronics Packaging (ICEP), Nara, Japan, 13-15 April 2011, pp. 986-990

B Investigation of accelerated surface oxidation of Sn-3.5Ag-0.5Cu solder particles by TEM and STEM

Xin, Luo; Wenhui, Du; Xiuzhen, Lu; Toshikazu, Yamaguchi; Jackson, Gavin; Lilei, Ye; Johan, Liu
Proceedings of the IEEE 2011 International Symposium on Advanced Packaging Materials (APM), Xiamen, China, 25-28 October 2011, pp. 73-79.
ISBN/ISSN: 978-146730147-3.
DOI: <http://dx.doi.org/10.1109/ISAPM.2011.6105674>

C Thermal performance characterization of nano thermal interface materials after power cycling

Shuangxi, Sun; **Xin, Luo**; Carl, Zandén; Björn, Carlberg; Lilei, Ye; Johan, Liu
Electronic Components and Technology Conference (ECTC), IEEE 62nd, San Diego, CA, USA, 29 May-1 June 2012, pp. 1426-1430.
DOI: 10.1109/ECTC.2012.6249023

D Study on the adhesion strength of new nano-structured polymer-metal composite for thermal interface material under different pressures

Lei, Zhang; Xiuzhen, Lu; **Xin, Luo**; Björn, Carlberg; Masoud, Zandira; Lilei, Ye; Johan, Liu
Proceedings - 12th International Conference on Electronic Packaging Technology and High Density Packaging, ICEPT-HDP 2011, Shanghai, China, 8-11 August 2011, pp. 426-429.
ISBN/ISSN: 978-145771768-0
DOI: 10.1109/ICEPT.2011.6066869

E Fabrication and characterization of a metal matrix polymer fiber composite for thermal interface material applications

Carl, Zandén; **Xin, Luo**; Lilei, Ye; Johan, Liu
International Conference of Thermal Investigations of ICs and Systems (THERMINIC), Berlin, Germany, 25 - 27 September 2013, pp. 286-292
ISBN/ISSN: 978-1-4799-2271-0
DOI: 10.1109/THERMINIC.2013.6675196

Abbreviations

3D	3-dimensional
AES	Auger electron spectroscopy
BF	Bright field
BN	Boron nitride
CMOS	Complementary metal oxide semiconductor
CNT	Carbon nanotube
CTE	Coefficient of thermal expansion
DF	Dark field
ENIG	Electroless nickel/immersion gold
FIB	Focused ion beam
FTIR	Fourier transform infrared spectroscopy
GB	Grain boundary
HAADF	High angle annular dark field
hBN	Hexagonal boron nitride
IMC	Intermetallic compound
InSnBi	Indium-tin-bismuth
ITRS	International technology roadmap for semiconductors
PCB	Printed circuit boards
PCMs	Phase change materials
PI	Polyimide
PVB	Polyvinyl butyral
SEM	Scanning electron microscopy
RTD	Resistance temperature detector
SnAgCu	Tin-silver-copper
STEM	Scanning transmission electron microscopy
TIM	Thermal interface material
TEM	Transmission electron microscopy
UTS	Ultimate tensile strength
XPS	X-ray photoelectron spectroscopy
XRD	X-ray diffraction

Table of contents

Abstract	III
List of publications	VII
Abbreviations	XI
1. Introduction	1
1.1 Background	1
1.1.1 Lead-free solder.....	1
1.1.2 Thermal interface material	2
1.2 Scope and outline	4
2. Characterization of nano-scale oxide of lead-free solder particles	5
2.1 Reviews of the Sn oxide studies.....	5
2.2 Characterization of nano-scale oxide of lead-free solder particles	6
2.2.1 TEM and STEM analysis	6
2.2.2 AES analysis.....	10
2.3 Summary and Discussion.....	12
3. Characterization of polymer fiber metal matrix composite-based TIM	13
3.1 Fabrication of polymer fiber metal matrix composite-based TIM.....	13
3.1.1 Composite design of TIM.....	13
3.1.2 Fabrication process and microstructure analysis.....	14
3.2 Thermal performance of polymer fiber metal matrix composite	20
3.2.1 Thermal conductivity tests	20
3.2.2 Thermal dissipation test system	21
3.2.3 Thermal reliability tests.....	24
3.3 Mechanical properties of polymer fibers metal matrix composite	25
3.3.1 Shear tests of PI fiber-InSnBi and PI fiber-indium composite.....	25
3.3.2 Tensile test of PI fiber-indium composite	28
3.3.3 Creep test of PI fiber-indium composite	36
3.4 Summary and Discussion.....	38
4. Characterization of thermally conductive fiber metal matrix composite-based TIM	41
4.1 Boron nitride fiber-indium composite-based TIM.....	41

4.1.1 Composite fabrication	41
4.1.2 Characterization of thermal performance	43
4.2 Carbon fiber-SnAgCu composite-based TIM	44
4.2.1 Composite fabrication	44
4.2.2 Characterization of thermal performance	45
4.3 Summary and Discussion	46
5. Conclusions and outlook.....	49
Acknowledgements.....	53
Bibliography	55

Chapter 1

Introduction

1.1 Background

The microelectronics packaging industry needs to continuously satisfy the demands of increasing performance, functionality and reliability while reducing size, weight and costs [1, 2]. With these requests, pivotal and new materials should be developed and investigated, for instance, lead-free solders and thermal interface materials (TIMs) [3, 4]. Lead-free solders and TIMs are widely used in the electronics packaging industry for interconnection and heat dissipation applications, respectively. The present thesis mainly focuses on the two research areas: nano-scale oxide analysis of lead-free solder particles and thermal/mechanical properties of nano-scale fibers metal matrix composite-based TIMs.

1.1.1 Lead-free solder

Lead-containing solder, such as SnPb alloy, has been a traditional material for assembly and interconnection in the electronics packaging industry for several decades. During the last decade, the solders have been modified due to a strong worldwide environmental movement towards non-toxic solders without lead [5]. Many initiatives and legislative measures outline the targets for the transition from lead-containing solders to lead-free types in the micro-electronic packaging application [6-8].

Many different lead-free solder alloy systems, such as SnAg, SnAgCu, SnCu, SnAgBi, have been developed as promising alternatives to SnPb solders [5]. Among these lead-free solders, the near eutectic Sn-3.8Ag-0.7Cu composition from the ternary SnAgCu system is presently the preferred one. This is mainly due to its relatively low melting temperature ($\sim 217^{\circ}\text{C}$), good solderability, high strength, low wetting angles and good reliability [9-11].

Despite numerous studies having reported on the promising lead-free solders in terms of the soldering process [12], Sn whiskers [12], interfacial reaction [13], reliability issues [14] and oxidation behavior of the soldered joints [15-17], a few studies of oxidation characteristics of a single SnAgCu solder particle have been reported. However, the composition and thickness of oxide of the solder particles are extremely important for solder joints and have a direct impact on the quality of interconnect and the reliability of a packaged system. Compared to Pb, the oxidation of Sn needs lower Gibbs free energy at room temperature, resulting in higher oxidation vulnerability of the Sn-based solders [18]. It is shown that even a small difference in the oxide thickness of lead-free solder powders would dramatically affect the performance of solder joints [19]. On the other hand, the study of Sn oxide is also motivated by the applications as a solid state gas sensor, oxidation catalyst, and transparent conductor [20].

1.1.2 Thermal interface material

With the development of packaging technologies, microelectronic products are increasingly moving towards higher power density in a limited packaging area, as shown in Figure 1.1.

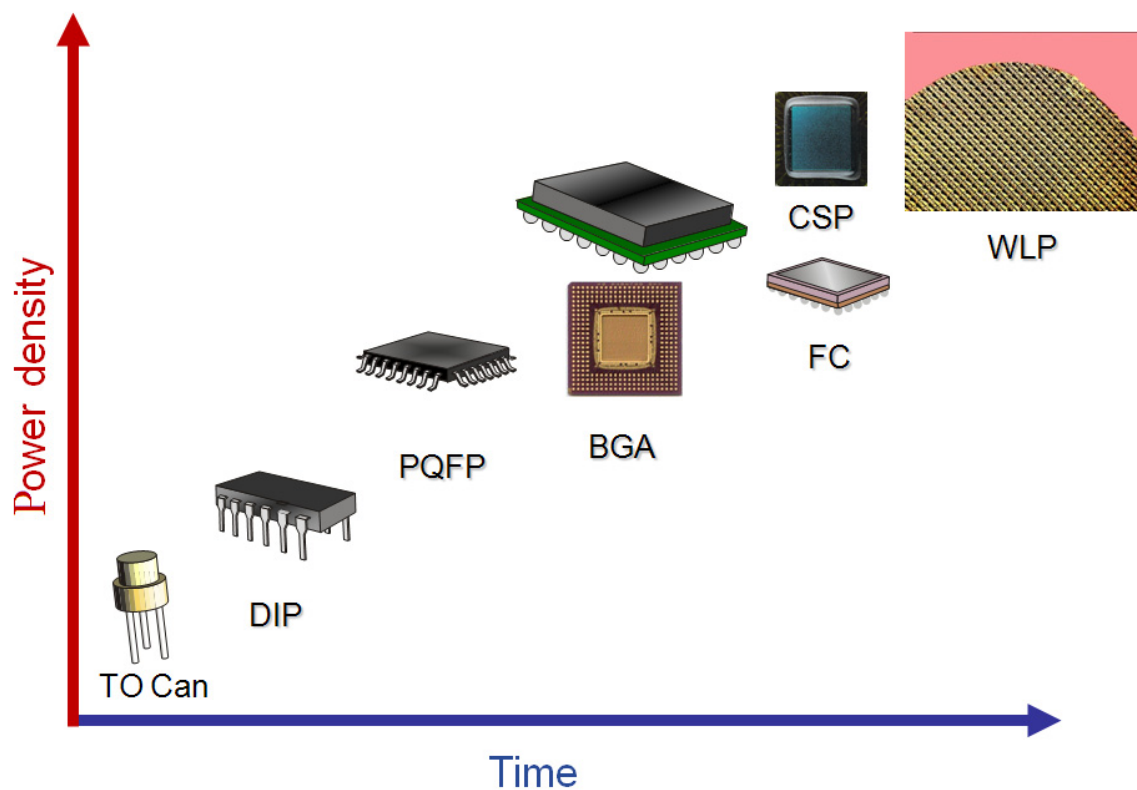


Figure 1.1: Schematic illustration of the trends towards higher power density with the development of micropackage technologies.

With this trend, power densities have reached magnitudes in the order of 100 W/cm^2 [21]. Figure 1.2 indicates the increasing junction temperature for electronic packaging in the future, in combination with increasing power densities. The development of microelectronic devices leads to increased junction temperature, resulting in severe deterioration behavior/failure in

semiconductors such as fracturing, delamination, melting, creep, corrosion, electromigration and even combustion of packaging materials. The problem is worsened further due to the presence of the hot-spots, localized areas on the chip that reach tremendous power densities during operation [22].

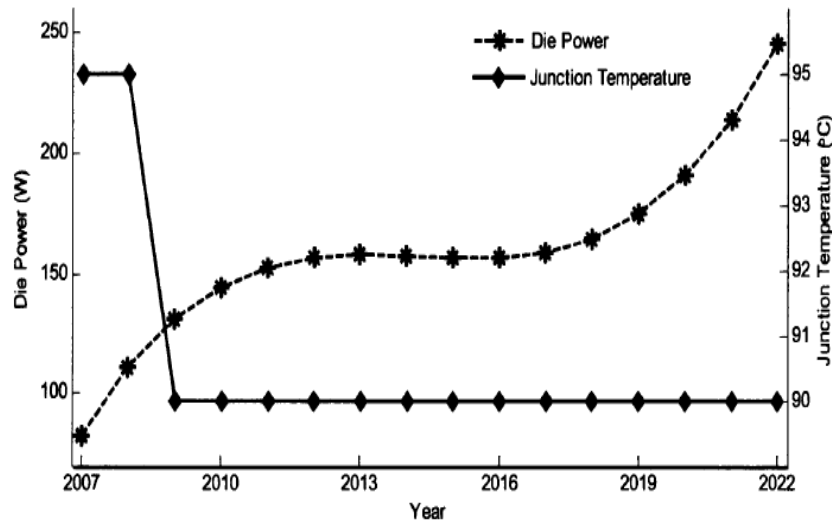


Figure 1.2: Projected microprocessor power dissipation (constant die area, 140 mm²) and junction temperature evolution [21].

The “high-flux hot-spots” are caused by miniaturization, design complexity and highly non-uniform power distribution on microprocessors. If the heat dissipated from the component does not spread out efficiently, hot-spot temperature may reach an unacceptable level, causing damage of electronic productions. For maintaining a relatively low junction temperature to improve the performance and long-term reliability of microelectronics systems, thermal management technologies are critical. Power delivery and thermal dissipation design in ever extending three-dimensional (3D) scaling are indispensable for further system integration. The thermal management challenges for assembly and packaging in future are also highlighted in the international technology roadmap for semiconductors (ITRS) report in 2013 [23]:

- *Thermal management for 3D assembly and packaging.*
- *Thermal dissipation for small die with high pad count and/or high power density.*
- *“Hot-spot” thermal management for high frequency die.*

Keeping a low and stable junction temperature at increased power densities in future applications requires a radically improved TIM. TIMs are used to fill the gaps between an electronic device and the thermal transfer medium such as the substrate, heat pipe, and heat sink, or join the thermal management components to each other. The air residing in the valleys in the surface topography is thermally insulating and should be displaced by the TIMs. In some cases, TIMs need to perform the functions of attachment, stress/strain relief as well as thermal transfer. TIMs have a significant impact on the thermal impedance of electronic systems and they can be the dominant factor in achieving effective thermal transfer in practice [24].

Currently available TIMs include thermal adhesive, greases, oils, non-metallic coatings, metallic foils and phase change materials (PCMs) [24-33]. In addition, composite TIMs are designed based on silicone or epoxy matrices dispersed with thermally conductive fillers, such as boron nitride [34-36], aluminum oxide [37], zinc oxide [38], aluminum nitride [39], nano-silicon carbides and silver nanowire arrays [40]. Furthermore, carbon allotropes have also been receiving increasing attention, such as carbon black [41], graphite [28], carbon nanotubes [42] and graphene [43, 44]. However, the limitation of the contents of the fillers influences the thermal conductivity of the composites. Furthermore, it is difficult to dispense the fillers uniformly within the matrix. Thermal oxidation aging can also cause significant weight loss in the polymer matrix, resulting in a filler loading change which can be exhibited by a prompt alteration in electrical resistivity and viscosity of the TIM [45].

To fulfill current and future thermal and thermomechanical requirements in the electronics packaging, the TIM requires heat transport at submicron scales, the compatible manufacturing processes used and the resiliency helping the conformability to the topography of the mating surfaces. In this sense, it is imperative to develop novel competent TIMs with improved thermal performance and long-term reliability in microelectronics systems. Secondly, it is important to control the dimension of the novel TIMs to satisfy the miniaturized package structure. Finally, the TIMs should be facilitated so as to be assembled or compatible with the current packaging process.

1.2 Scope and outline

The thesis is organized into 5 chapters. Chapter 1 presents a general introduction about lead-free solders and TIMs. Chapter 2 emphasizes the analysis of the nano-scale oxide of the solder particles. The oxide thickness of solder powders is investigated by transmission electron microscopy (TEM) and scanning transmission electron microscopy (STEM). Chapter 3 is devoted to the preparation and characterization of a new class of TIMs, the nano-scale fiber metal matrix composite, including polyimide (PI) fiber-InSnBi, PI fiber-indium and PI fiber-SnAgCu composite. Chapter 4 introduces the fabrication and characterization of boron nitride (BN) fiber-indium and carbon fiber-SnAgCu composite. The outlook and conclusions are given in chapter 5.

Chapter 2

Characterization of nano-scale oxide of lead-free solder particles

In this chapter a general introduction about the oxide studies of Sn materials, including the sample preparation, applied equipment and basic results is described. Afterwards, the results from the TEM and STEM deployed to directly observe the nano-scale oxide of lead-free solder particles are presented.

2.1 Reviews of the Sn oxide studies

One of the eldest studies related to the thickness measurement of the Sn oxide film is done by coulometric and polarization methods [46, 47]. However, these methods are not suitable for the micron-sized lead-free solder particles. Auger Electron Spectroscopy (AES) has been later developed and employed for in-depth analysis of Sn oxide [19, 48, 49]. This measurement could provide an oxygen concentration-depth curve, but the criterion to determine the thickness of oxide is arbitrary. For instance, a whole oxygen containing layer is denoted as “oxide film” in ref. [48] while ‘half-height’ of oxygen is considered as an estimate of the oxide-substrate interface in ref. [19, 49].

Beside the investigation into the oxide thickness, the chemical composition of the oxide is another important issue. Although only two Sn-O compounds, Sn_3O_4 and SnO_2 , are presented at room temperature according to the Sn-O phase diagram (Figure 2.1), the composition of Sn oxide is proved more complex in practice. SnO and SnO_x ($0 < x < 2$) have also been reported when the oxidation of Sn is incomplete [50-52]. Yuan et al have reported that the outermost Sn oxide phase is SnO , and that the SnO phase would eventually transform into SnO_2 phase after prolonged annealing [50]. Hart et al have examined the oxidation process of a thin Sn foil in-situ by electron microscopy [51]. The resulting electron diffraction patterns reveal that there

is a gradual transition of Sn oxide (Figure 2.2), through an amorphous oxide in the cooler regions and a crystalline SnO stage to the higher valency oxide, SnO₂.

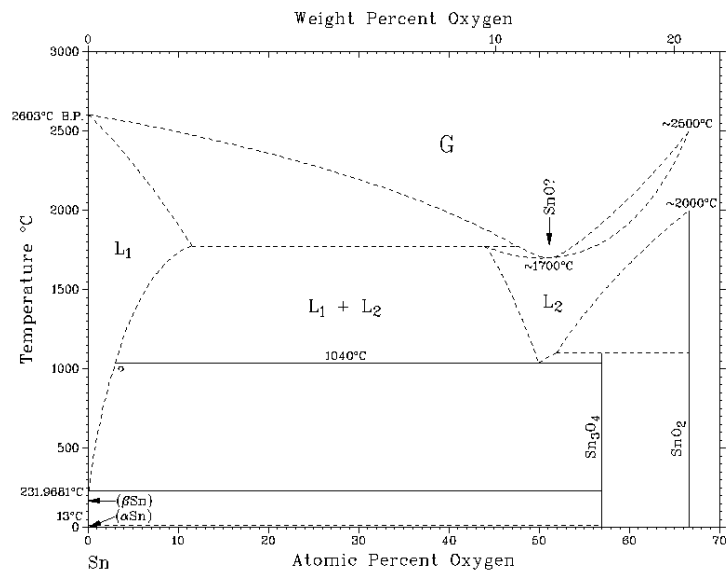


Figure 2.1: Binary Sn-O phase diagram [53].

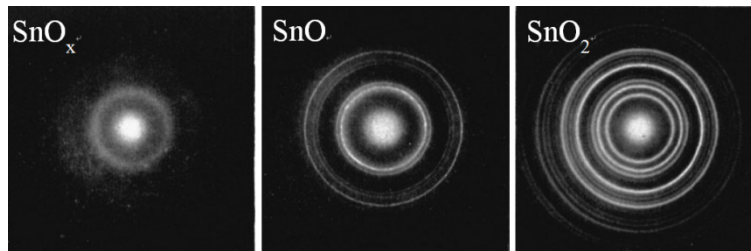


Figure 2.2: Electron diffraction patterns of Sn oxide transitioned with oxidation time [51].

2.2 Characterization of nano-scale oxide of lead-free solder particles

2.2.1 TEM and STEM analysis

Lead-free solder particles of Sn-3.5Ag-0.5Cu (wt.%) are provided by the Henkel Technologies Company. The shape, size and dimensional distribution of the solder particles are shown in Figure 2.3. The particles are almost spherical and their diameters range from 5 to 35 μm . To study the oxide growth, these powders have been exposed to air (70% relative humidity) and heated to 150 $^{\circ}\text{C}$ for 0, 120 and 240 h, respectively.

Because conventional techniques for TEM sample preparation, such as electrolytic jet thinning or ultramicrotome, are unsuitable for the micro-scale particle sample, focused ion beam (FIB) technology has been employed to avoid destroying or changing the solder oxide. First, the solder powders are cleaned in acetone by ultrasonication for 10 min to remove any surface contamination, then they are mixed with resin and the mixture are inserted into a 3 mm diameter Cu tube. After completely cure of the resin, the solder-filled Cu tube is cut into slices with 0.5 mm thickness and thinned down to 0.05 mm with grinding and denting machines.

Finally, the Cu tube is removed mechanically, and the sample is affixed to a common carbon film TEM carrier with a specific TEM-use adhesive. The FIB system has been used to etch the sample to about 100 nm in thickness. It is worth noting that the solder powders are filtrated from a 500# stainless steel strainer (with holes of 25 μm diameter) before the TEM sample preparation. The purpose of the filtration is to make the particles' dimension uniform and make sure the observed cross section of the solder powders is nearly equal to their radial section

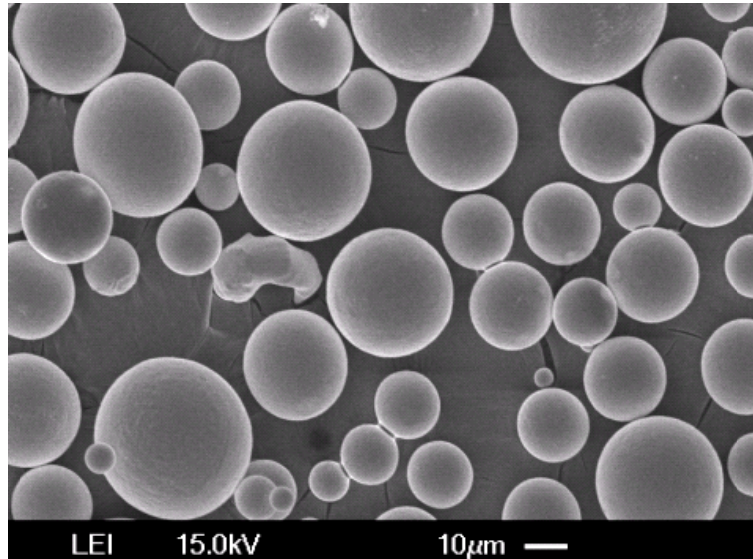


Figure 2.3: Scanning electron microscope (SEM) image of the pristine lead-free solder particles.

High-angle annular dark-field scanning transmission electron microscopy (HAADF-STEM) analysis is quite a new technique as a hybrid test performed on modified TEM, which is originally proposed by Howie [54] in the 1970s and rapidly developed in the 1990s [55]. Its generic principle is illustrated in Figure 2.4 [56]. The electrons transmitted from the sample that are illuminated by the scanning beam may be divided into three regions based on their interactions with the specimen. These regions can be visualized as three coaxial cones of increasing angularity whose common vertices are at the point of transmission. The central and intermediate cones could be detected as the bright field (BF) and dark field (DF) images, respectively. The third and widest cone contains electrons that have been scattered through high angles by interactions with the atomic nuclei in the sample. The intensity of this signal is primarily a function of the sample's atomic number. Images formed from this are known as Z-contrast images. Therefore, the contrast of HAADF images is strongly dependent on the average atomic number of the sample, which could be used to distinguish the oxide of solder particles from the pure matrix metal.

TEM image of the pristine sample of the solder particle without oxidation treatment is shown in Figure 2.5, in which the white (left) region corresponds to the SnAgCu matrix; the narrow grey (middle) domain corresponds to the oxide layer and the dark (right) region corresponds to epoxy. The interface between the solder matrix and oxide layer is clearly visible. The thickness of the oxide layer is around 5 nm. From Figure 2.6, the thickness of the oxide layer of the solder sample with 120 hours of thermal oxidation is measured at about 50 nm. The 120 hour oxide growth sample is also tested by line scanning analysis to confirm oxide

layer location. The red line in the top left sub-graph in Figure 2.7 indicates the scanning path across the oxide layer. The distribution of the oxygen element shows an oxygen-rich platform indicated by a double arrow line corresponding to the oxide layer (see Figure 2.7). The width of the region is also about 50 nm.

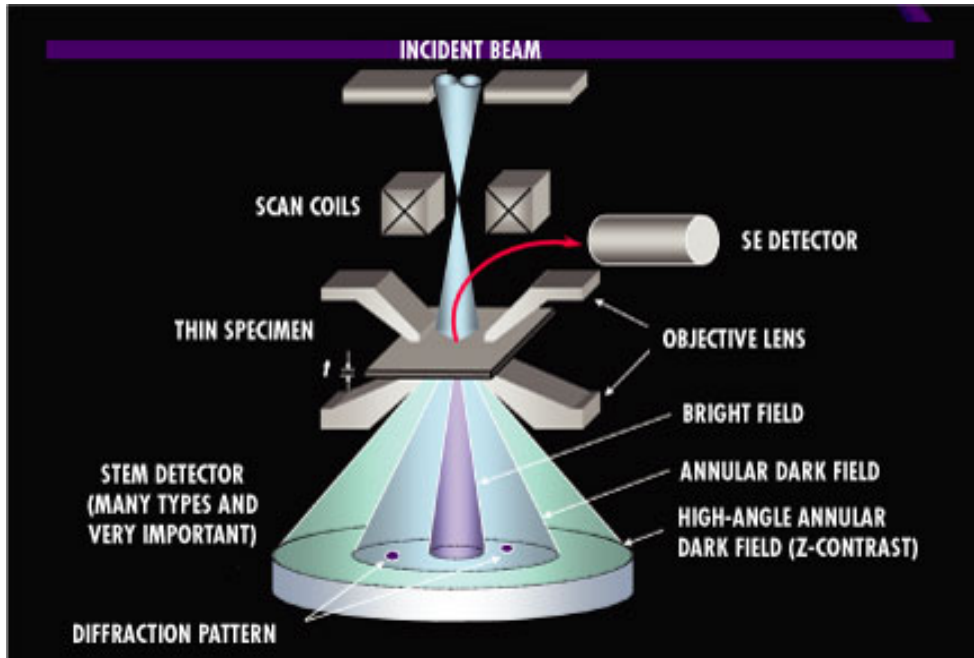


Figure 2.4: Illustration of the bright-field, dark-field, and high-angle annular dark-field functions of a STEM [56].

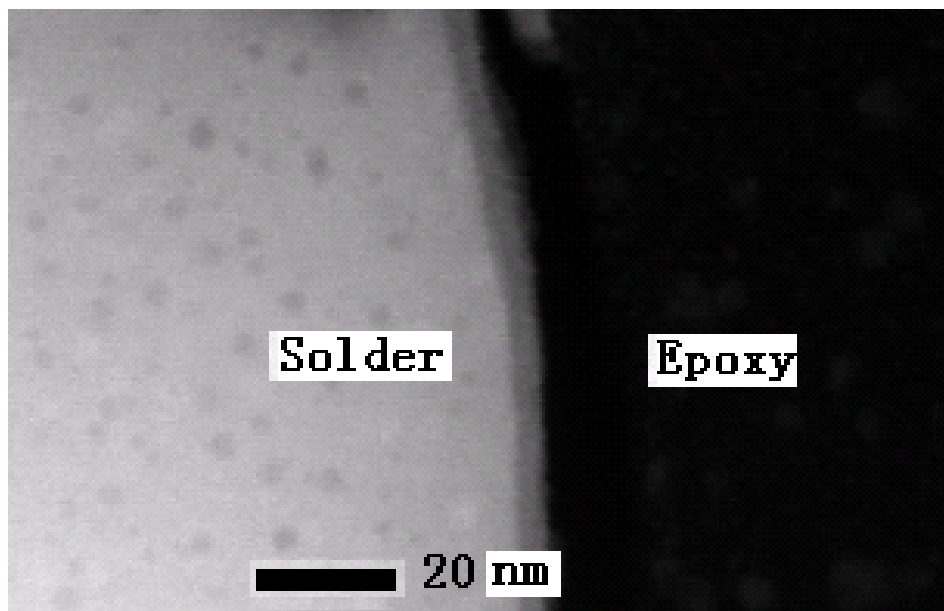


Figure 2.5: HAADF-STEM image of oxide layer of the pristine solder particles with 0 h oxidation growth.

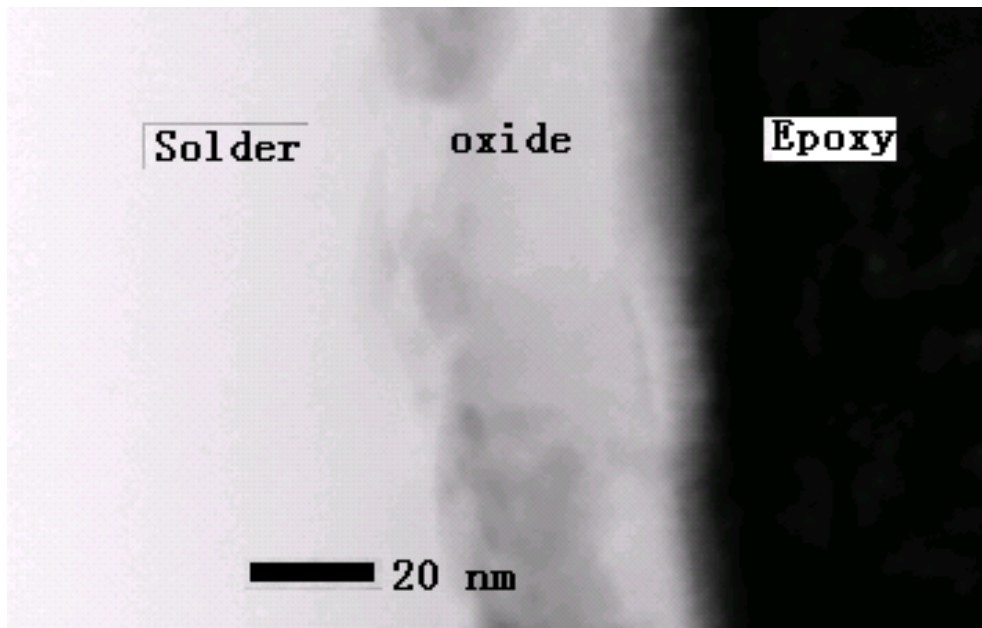


Figure 2.6: HAADF-STEM image of oxide layer of the solder particles with 120 hours oxidation growth.

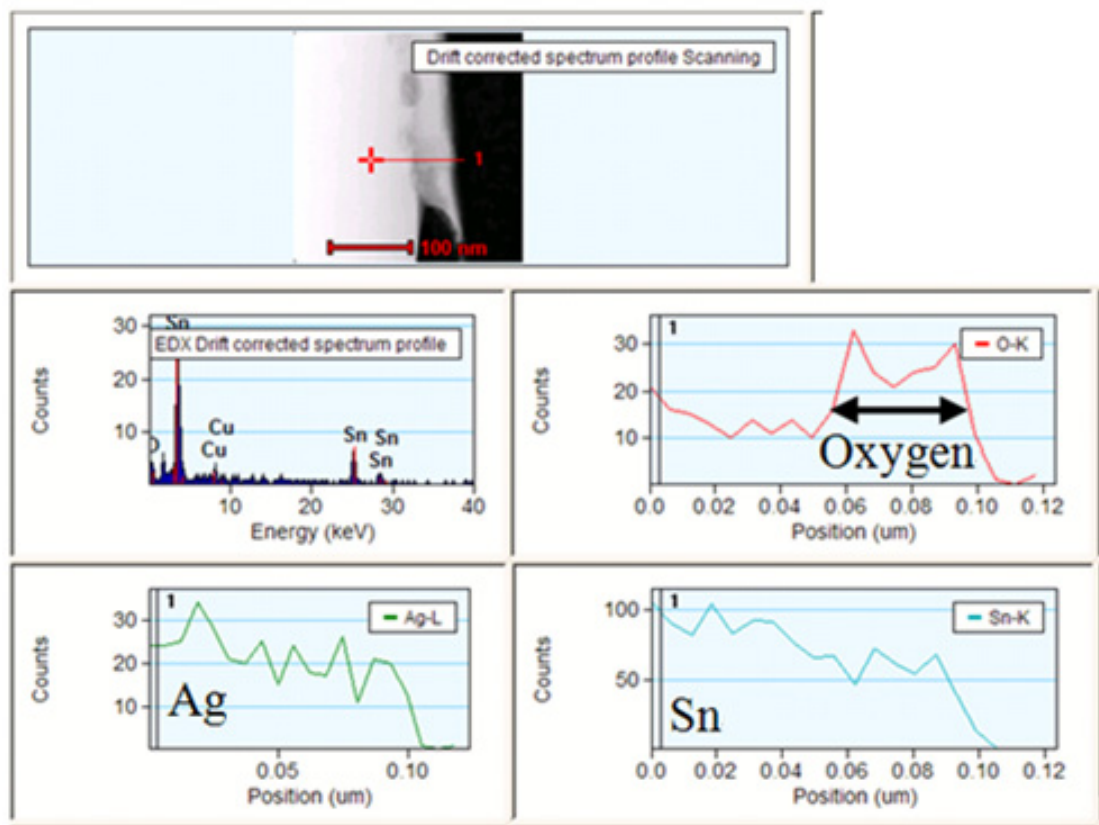


Figure 2.7: STEM analysis of the oxide layer of the solder particle with 120 hours oxidation growth.

2.2.2 AES analysis

AES is a non-destructive and nano-scale distinguished electron spectroscopy for semi-quantitative determination of the elemental composition of surfaces, thin films and interfaces [57]. AES can be used for depth profiling with simultaneous ion sputtering. The principle of the spectroscopic technique underlies the Auger effect, discovered by Pierre Auger [58], which is based on the analysis of energetic electrons emitted from an excited atom after a series of internal relaxation events.

As mentioned in section 2.1, because of a lack of clear metal-oxide interface, it is difficult to determine the thickness of the oxide layer from the oxygen concentration-depth profile detected by AES. Neither the ‘all oxygen’ method [48] nor the ‘half-height’ method [19, 49] is correct in terms of our TEM results (Figure 2.5 and 2.6). Herein, an intersection analysis method for the AES results is introduced. As shown in Figure 2.8, tangent lines of the initial downward slope and the baseline of the oxygen curve intersect at a point (indicated by a black dot) which could be recognized as the location of the solder matrix-oxide layer interface. For the pristine sample (Figure 2.8) and the 120 hour oxide growth sample (Figure 2.9), the thicknesses of their oxide are 5 nm and 50 nm, respectively, according to the intersection method. For 240 hour oxide growth sample, the oxide thickness is about 70 nm via the same method (Figure 2.10).

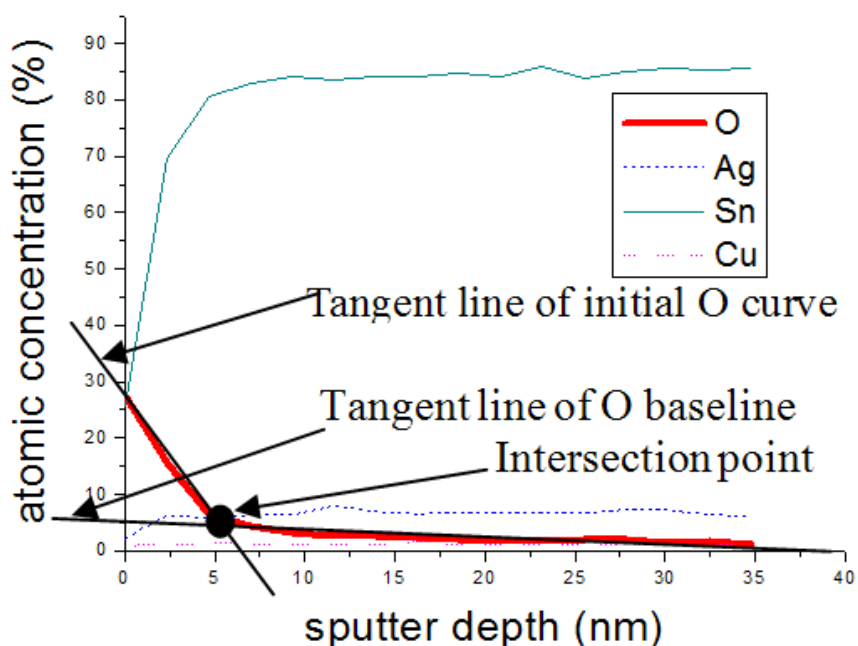


Figure 2.8: AES depth profiles for the pristine solder particles with 0 hours oxidation growth. Thin line indicates Sn, thick line indicates O, dashed line indicates Ag and dotted line indicates Cu. (These indications are the same in Figure 2.9 and 2.10)

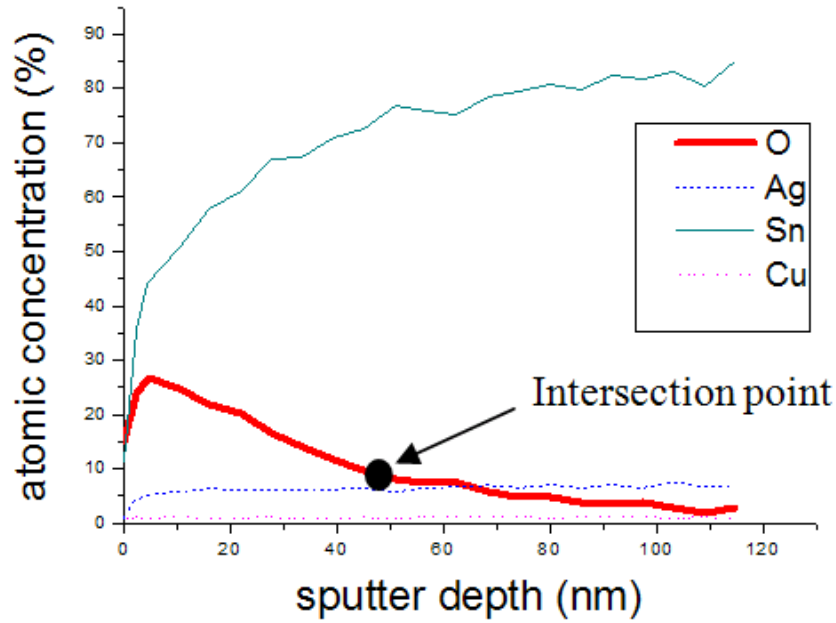


Figure 2.9: AES depth profiles for the solder particles with 120 hours oxidation growth.

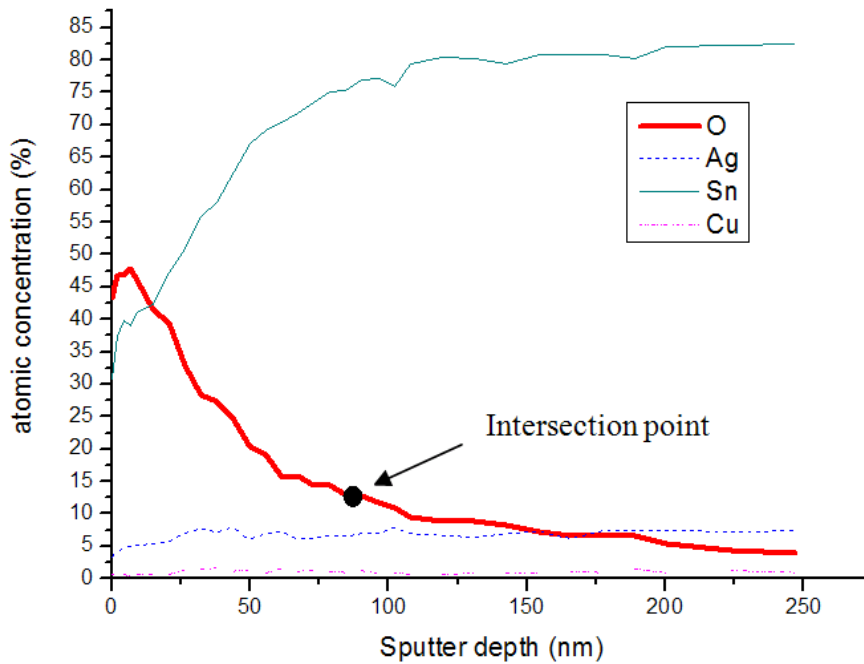


Figure 2.10: AES depth profiles for the solder particles with 240 hours oxidation growth.

Figure 2.11 shows the relationship between the oxide thickness and the oxidation time of the solder particles in our case. The thickness is proportional to the square root of the oxidation time with a high degree of confidence. It is believed that the oxide growth is controlled by the diffusion of oxygen [59, 60].

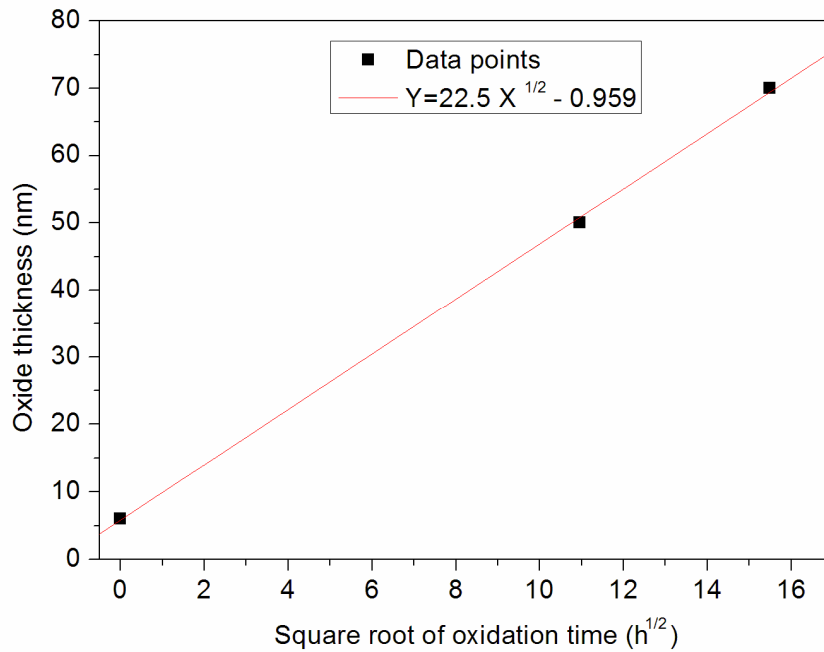


Figure 2.11: Increase of oxide thickness as a function of oxidation time for lead-free solder particle at 150 °C.

2.3 Summary and Discussion

In conclusion, the thickness of the oxide layer in micro-dimensional solder particles has been studied by TEM, STEM and AES technologies, respectively. An intersection analysis for AES profiles is introduced to determine the oxide thickness of the solder powders. The surface oxide thickness is proportional to the square root of the oxide growth time. Though requiring more care in sample preparation, the measurements by TEM and STEM are more direct and precise.

Chapter 3

Characterization of polymer fiber metal matrix composite-based TIM

This chapter is to introduce and characterize the TIMs based on electrospun PI fibers and different infiltrated metal matrices. Section 3.1 introduces the composite design of the novel TIMs and their fabrication processes. Section 3.2 studies the heat dissipation performance of the PI fiber-indium composite-based TIMs. Afterwards, the mechanical properties of the composite are investigated in section 3.3.

3.1 Fabrication of polymer fiber metal matrix composite-based TIM

3.1.1 Composite design of TIM

There is a critical need for TIMs to spread heat from logic components or chips in multi-chip packages. Generally, the TIM used between the heating unit and heat spreader is called TIM1 and TIM2 is sandwiched between the heat spreader and heat sink. A typical heat spreader or heat sink is constructed of Al or Cu with high thermal conductivity. The coefficient of thermal expansion (CTE) mismatch between Al or Cu and Si chips requires that the TIM should absorb strain as well as dissipate heat. As mentioned before, with the development of increasing transistor integration and sophisticated packaging technologies, polymer-based TIMs cannot fulfill the urgent demands for thermal conduction in high-power electronic packaging because

of their low thermal performance in the 4-5 W/mK range [4, 24, 29, 31, 33]. Consequently, metal matrix based TIMs have been attracting considerable attention.

The choice of metal is always the lead-free solders due to their inherent high thermal conductivity (one order of magnitude larger than polymer-based TIMs), compatible assembly technologies (same soldering conditions in reflow), negligible contact resistances (fill all gaps by melting solder) [61]. Numerous solders have been extensively employed in thermal dissipation applications, namely die attach materials of power semiconductors. Generally, the higher the bond strength, the better the thermal dissipation [62]. However, the large mechanical strength in the solder joint results in severe stress at the interface, especially during the thermal cycling. The thermomechanical issue is chronic for the SnAgCu solders because this solder has large modules and very low ductility. The feasibility of indium as a TIM has been considered [63, 64], including by Advanced Micro Devices (AMD) [65] and Intel cooperation [66]. Indium exhibits superior thermal performance due to its high thermal conductivity (82 W/mK) and excellent wettability with most surfaces [67]. In addition, the high ductility of indium is favorable for relieving mechanical stress caused by CTE mismatch between the heat spreader and silicon chip [68, 69]. Furthermore, the low melting temperature (T_m) of indium (156 °C) makes the reflowing temperature lower in comparison with tin-based lead-free solder, which benefits the packaging of fragile, thermally sensitive next-generation devices containing polymers, nano- or biomaterials [70]. However, pure indium suffers from easy deformation due to a very low normal yield strength (1~2 MPa) [68]. It also has poor creep resistance during both handling and usage, especially at high temperatures [71].

The mechanical problem of these solders can be circumvented by introduction of polymer fiber networks to adjust the mechanical properties [72, 73]. With the introduction of the polymer fibers, the stiffness of the SnAgCu matrix composite decreases and the strength of the indium matrix composite increases. The choice of the thermosetting PI material is due to its excellent mechanical properties, good thermal stability, low water absorption and excellent corrosion resistance. [74-76]. The ultimate tensile strength (UTS) of PI materials is in the range of 100 MPa [77]. At the nanoscale, it is reported that the PI nanofiber (300 nm in diameter) has an average UTS of 1.7 GPa and axial tensile modulus of 76 GPa [78]. Besides the fiber itself, there are many advantages for the composite design. Firstly, the polymer fiber network in the composite design could be tailored to various sizes to satisfy the sophisticated requests in microelectronic production and its thickness could be controlled. Secondly, the thickness of fibers film provides a certain space for the melting metal to avoid the outflow issue. Finally, the introduction of the fibers could absorb thermomechanically induced strain to improve the reliability of metal based TIMs. The polymer fiber-indium composite for large scale usage is also cost-effective compared to the pure indium TIM.

3.1.2 Fabrication processes and microstructure analysis of polymer fiber-metal matrix composite

The polymer fiber-metal matrix composites are fabricated using a procedure including three main steps as shown in Figure 3.1.

1. The polymer fibers are electrospun from PI (Matrimid 5218, Huntsman Advanced Materials) dissolved in N, N-Dimethylacetamide (DMAC) (Sigma-Aldrich). Electrospinning is performed at a voltage of 20 kV, a feed rate of 2 mL/h and a 20 cm distance between the cannula and the collector (Nanofiber Electrospinning Unit, Kato).

2. To improve the wettability with metal/alloy, the PI fiber network is rinsed in absolute ethanol followed by DI water to wash off organic residues. The mesh is then immersed in 4 M KOH aqueous solution at 80 °C for 30 min to induce imide-ring cleavage and form a potassium polyamate layer in the polymer chains on the surface of each fiber. After rinsing with DI water, the fibers are immersed in 100 mM AgNO₃ aqueous solution at room temperature for 30 min to induce an ion exchange process in which the bound potassium ions are replaced by silver ions. Following another rinsing with DI water, the Ag⁺ ions are reduced to form a silver coating on the fiber surface by immersion in 1 mM DMAB aqueous solution at room temperature for 30 min. After a final rinsing in DI water, the residual layer of polyamic acid is re-imidized through a thermal treatment in a nitrogen atmosphere at 350 °C for 30 min.

3. Finally, the surface functionalized nanofiber structure is placed in the evacuated mould cavity of our homemade squeeze casting system. The mould temperature is raised to a high temperature and infiltration of the liquid metal is carried out at 30 MPa pressure (maintained for 10 seconds) [73]. The subsequent mould cooling relied on cycling water at a cooling rate of about 20 °C/min. Generally, the applied temperature during infiltration is 20 °C higher than the melting point of the chosen metal. There are three types of metal applied as shown in table 3.1.

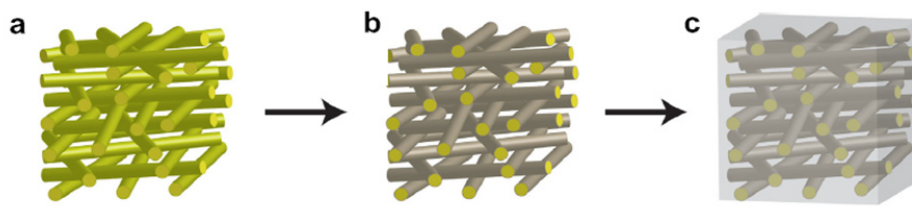


Figure 3.1: Schematic illustrating the principal structure and functionality of the developed PI fiber metal matrix composite-based TIMs. The fiber carrier formed by electrospinning (a), surface modification on the fiber (b), and pressure-assisted infiltration of metal matrix (c).

Table 3.1: Infiltrated metal for PI fiber metal matrix composite-based TIM.

Infiltrated metal	Melting point	Operating temperature for the TIM	Specification
InSnBi	60°C	<50°C	<ul style="list-style-type: none"> • Step soldering • Temperature-sensitive components, i.e. fusible alloys/fuse applications, plastic device, bio-device
Indium	157°C	<140°C	<ul style="list-style-type: none"> • Step soldering • General usage providing high thermal conductivity
SnAgCu	220°C	<200°C	<ul style="list-style-type: none"> • Compatible with lead-free soldering technology

Figure 3.2a displays a SEM image of the resulting electrospun PI fibers with random orientation and 3D fibrous network. The mean diameter of the fibers is approx. 780 nm (std. dev. 240 nm). The insert picture in Figure 3.2a shows the PI film electrospun with a large size. In contrary to the smooth surface of a single PI fiber shown in Figure 3.2b, compact and uniform Ag nanoparticles are coated on the surface of the fiber after surface modification (Figure 3.2c). Figure 3.2d reveals that high porosity fiber networks are infiltrated by indium. The insert in Figure 3.2d shows the final PI fiber-indium composite. The thickness of the composite is about 0.05 mm and mechanical test specimens are cut from the film. Figure 3.2e and f show the final PI fiber-InSnBi and PI fiber-SnAgCu composite, respectively. Clearly, interspaces among fibers are all filled by infiltrated metal, creating a composite with a continuous metal phase in a fibrous polymer phase.

The microstructural details of the PI fiber-indium composite have been investigated thoroughly. An X-ray diffraction (XRD) patterns collected in Figure 3.3 confirm the deposition of Ag and the peak in the range of 15° ~ 30° indicates amorphous structure of the fibers. The composite shows the characteristic peaks of indium without deviation from the standard sample of indium, indicating no lattice deformation or inner stress inside the composite material.

The TEM samples of the PI fiber-indium composite are fabricated by an analytical dual beam FIB system (Nova 600 NanoLab, FEI) with a Ga^+ ion beam current of 7 nA at 30 keV. Figure 3.4a shows a site-specific region with a protective platinum layer along a PI fiber; trenches are then milled on both sides of the fiber to create a 5 μm thick foil as shown in Figure 3.4b. Next, the TEM foil is attached using a micromanipulator (Figure 3.4c), and lifted out after separation from the bulk. Finally, the TEM foil is transferred to a fixture assembled in a single tilt-straining holder, and a final FIB etching is performed to obtain about 100 nm thickness (Figure 3.4d). Using the single tilt-straining holder, the TEM foil can be also tested by the in-situ TEM straining analysis.

In order to investigate interfacial information between the PI fiber and infiltrated metal, the FIB-fabricated TEM foil in Figure 3.5d is detected by STEM to show the HAADF imaging at a fiber-indium interface. BF TEM imaging, selected area electron diffraction (SAED) and energy dispersive X-ray detector (EDX) are employed to analyze the fiber, indium and their interface, respectively. Figure 3.5 shows the BF TEM and STEM images at the same location. In Figure 3.5a, a fiber's cross section appears as white while indium appears as black. EDX analysis inside the fiber (area 1 in Figure 3.5a) shows traces of Ag resulting from its penetration during surface modification. The Ag nanoparticles are also confirmed by polycrystalline rings in the SAED of area 1. From the EDX results in area 2, the interfacial layer is believed to consist of an IMC layer of AgIn_2 [79] which is also confirmed by the diffraction pattern of area 2. A Z-contrast HAADF-STEM image (Figure 3.4b) reveals the interface more clearly, in which the fiber is black while indium is white. The grey part (as shown between dash lines in Figure 3.5b) between them is estimated to be an interfacial layer with a thickness of about 50 nm. In area 3, EDX analysis shows 100% indium as expected, and the diffraction pattern also shows the orientations of indium.

Figure 3.6 shows the morphology of the TEM sample of the PI fiber-SnAgCu composite. Figure 3.6a is the overview of the sample with the solder alloy (black contrast) on the left side and polymer fiber (white contrast) on the right side. With a close look at the interface between the SnAgCu matrix and PI fiber, two different morphologies are detected: an interfacial layer as shown in Figure 3.6b and a direct contact area between the solder and polymer fiber in Figure 3.6c. It seems that the formation of the IMC layer is not continuous along the interface,

indicating that some of the Sn dissolves into Ag during the infiltration process. From the solder part, the precipitated Ag_3Sn and Cu_6Sn_5 particles are observed on the Sn matrix as shown in Figure 3.6d, which is the typical microstructure of a SnAgCu alloy.

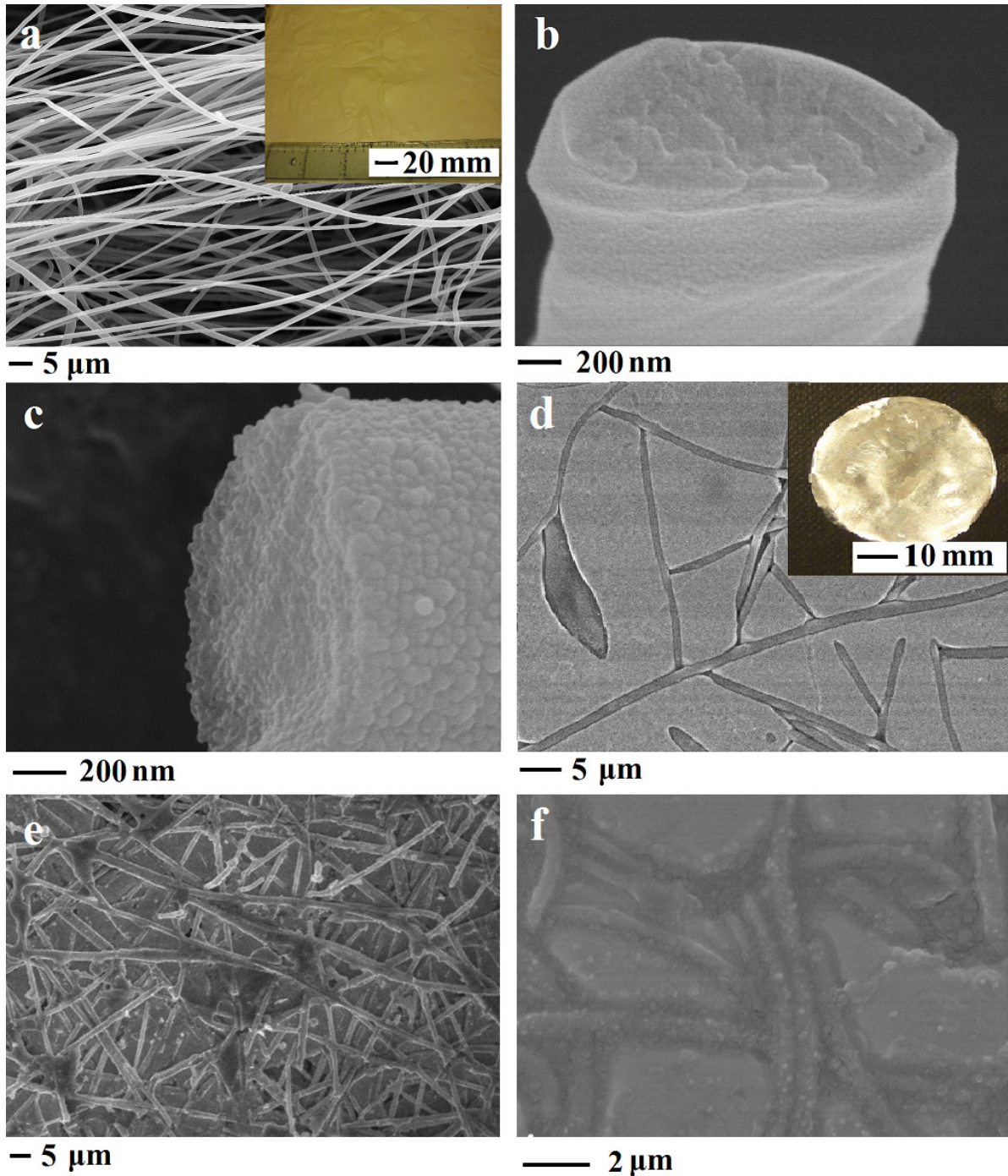


Figure 3.2: SEM images of electrospun PI fibers (a), a single PI fiber (b), an Ag-coated PI fiber (c), PI fiber-indium composites (d), PI fiber-InSnBi composite (e) and PI fiber-SnAgCu composite (f). The inserts in (a) and (d) are digital images of the electrospun fiber film and PI fiber-indium composites.

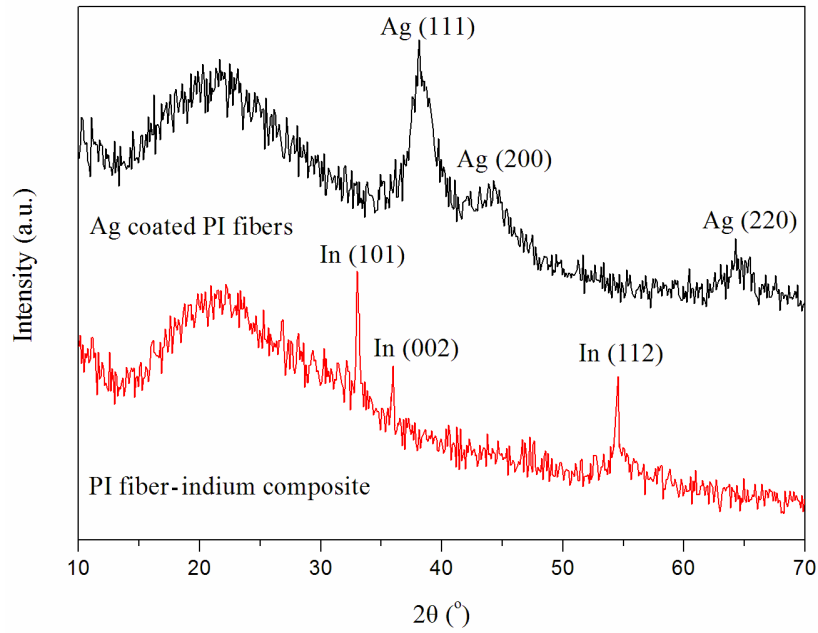


Figure 3.3: XRD diffraction patterns from Ag-coated PI fibers and PI fiber-indium composite.

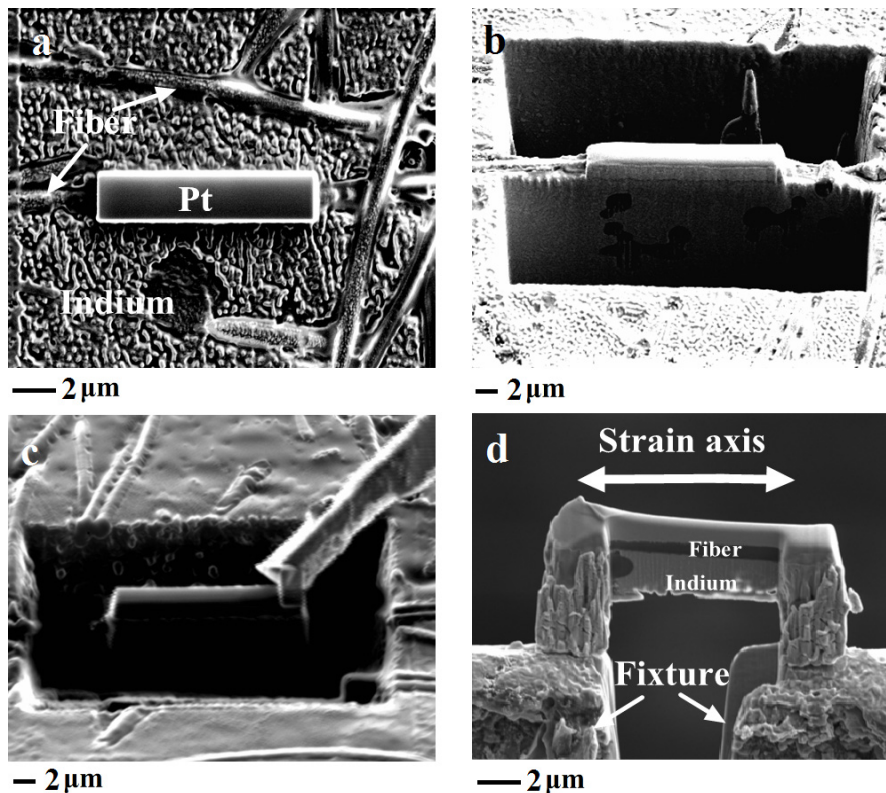


Figure 3.4: SEM images of FIB fabrication steps for the preparation of the in-situ TEM straining sample showing the chosen area with Pt deposition (a), cutting the side trenches (b), attaching with micromanipulator tip for lift-out (c) and the final sample attached to a fixture in a single tilt straining holder (d).

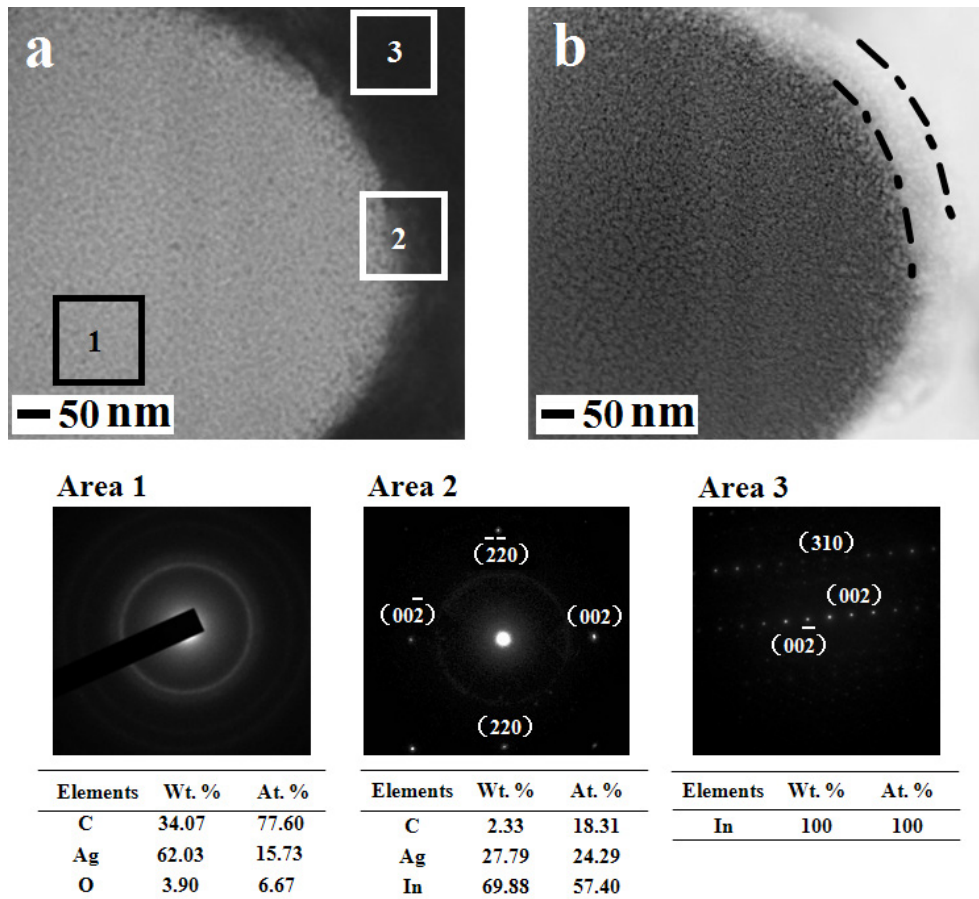


Figure 3.5: BF TEM (a) and HAADF STEM images (b) at the same interface between Ag-coated PI fiber and indium. Boxes in (a) indicate different areas for SAED and EDX analysis and dash lines in (b) indicate the interfacial layer of the composite.

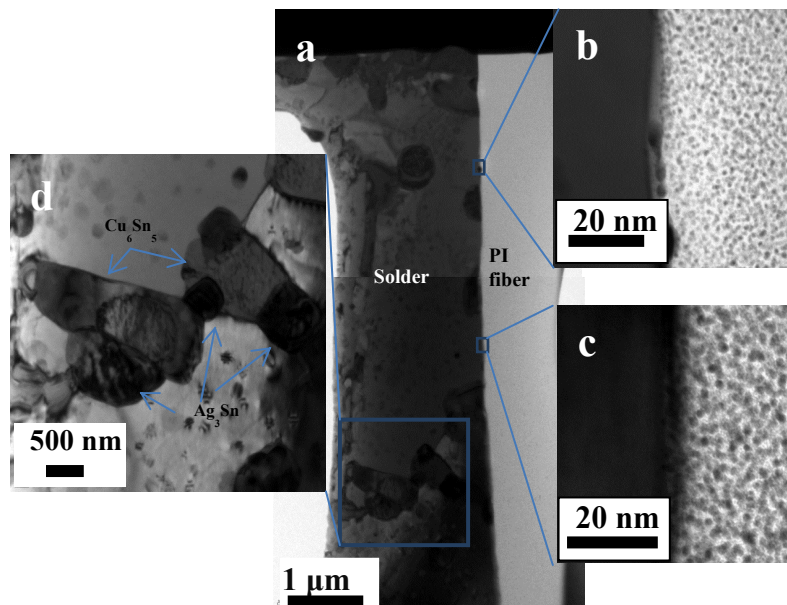


Figure 3.6: TEM images of PI fiber-SnAgCu composite (a), fiber/SnAgCu interfaces (b, c), and SnAgCu matrix (d).

3.2 Thermal performance of polymer fiber metal matrix composite-based TIM

3.2.1 Thermal conductivity tests

Thermal conductivity measurements for the polymer fiber metal matrix composite-based TIM are employed using a xenon flash instrument (LFA447 Nanoflash, Netzsch Gerätebau GmbH) [80]. In this transient non-contact method, the sample is subjected to a short energy pulse on one side and the temperature rise on the opposite side is recorded with an InSb infrared detector. From the characteristics of the detected transient temperature, the thermal diffusivity (α) of the tested material can be evaluated, and the thermal conductivity (K) can be obtained via the expression:

$$K = \alpha \rho C_p$$

where ρ is the density and C_p is the specific heat of the sample.

On the other hand, the through-plane thermal conductivity of the composites is calculated using Lee's methodology, the proportional relationship between the total thermal resistance and bondline thickness [81]. Several samples of the composite with different thicknesses are sandwiched between two copper plates ($8 \times 8 \text{ mm}^2$, 1 mm in thickness) by reflow (180 °C for the fiber-indium composite and 250 °C for the fiber-SnAgCu composite, 80 s, at 200 kPa pressure). Before the reflow, each copper and TIM is immersed in hydrochloric acid (10% vol.) for 1 min and rinsed with deionized water to remove oxides. The total thermal resistance (R_{Total}) between the two Cu plates includes the thermal resistance of TIM (R_{TIM}) and the contact resistances ($2R_{\text{contact}}$) between the TIM and Cu. By varying the thickness of the TIM as an intermediate layer, the interfacial thermal resistance can be extracted by linear regression of R_{Total} versus the thickness (d):

$$R_{\text{Total}} = R_{\text{TIM}} + 2R_{\text{contact}} = d/k + 2R_{\text{contact}}$$

Figure 3.7 sums up the results of the measured thermal conductivity of the polymer fiber metal matrix composites with different matrices. It can be understood that the thermal conductivity of the composite are related to its infiltrated metal matrix.

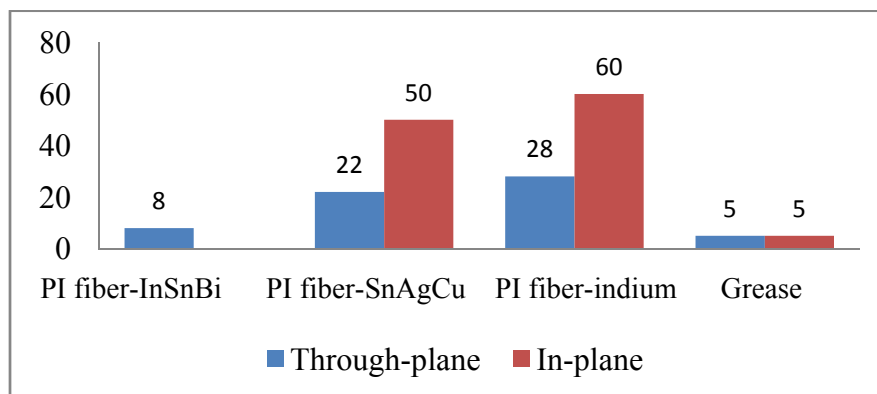


Figure 3.7: Thermal conductivity results of these polymer fiber metal matrix composites compared to a commercial grease TIM.

3.2.2 Thermal dissipation test system

In order to study the thermal performance of the PI fiber-indium composite for in-situ industrial applications with various dimensions, thermal test chips of different sizes are fabricated. 5×5 , 10×10 , 20×20 and 30×30 mm² chips are designed on a 3-inch wafer, as shown in Figure 3.8. Resistance temperature detectors (RTDs) composed of Ti/Pt/Cu (20/40/40 nm) are fabricated on the surface of the Si wafer via standard photolithography, electron beam evaporation and lift-off processes. It is conceivable that a larger stress exists on the interface when a larger sized TIM is used. The RTDs act as heating components to simulate the hot-spots of the chips in operation, and this testing system is used to monitor and record the hot-spot temperatures.

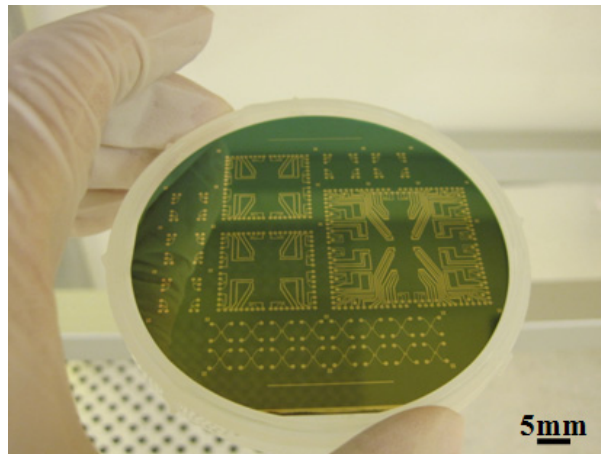


Figure 3.8: Layout of the test chips with various sizes and RTD designs fabricated on a 3-inch wafer.

According to the dimensions of the test chips, four different heat spreaders are fabricated using a high thermal conductivity alumina materials. In the center of the heat spreaders, there are square pads of 5×5 , 10×10 , 20×20 and 30×30 mm², respectively, metalized via the electroless nickel/immersion gold (ENIG) process for Au wire bonding as shown in Figure 3.9. The sandwich-like thermal dissipation testing system is designed as shown in Figure 3.10, which considers one dimensional heat flow path through the TIM layer from the test chip to the heat spreader. To assemble the system, Ti/Au (20/100 nm) layers are sputtered onto the back of the chip to form metallic bonding with the TIM. Indium-dedicated flux (Tacflux012, Indium Corporation) is screen-printed on the central area of the heat spreader and the back of the chip. The TIM films sandwiched between the test chips and heat spreaders subject to a reflow process (90 s, 180 °C) at 200 kPa pressure. The chips and heat spreaders are connected by wire bonding with Au wire (25.4 μ m diameter). Figure 3.11 shows the packaged testing systems. Commercial thermal grease is also sandwiched on a 5×5 mm² test frame for reference.

The junction-to-case thermal resistance (R_{thJC}) can be determined by the heat dissipation testing system, which is defined as:

$$R_{thJC} = (T_J - T_C) / P$$

where T_J is the junction temperature of the chip measured by the RTD components, T_C is the case temperature, tested by a thermocouple placed on the bottom surface of the heat spreader. P is the heating power of the chip controlled by a voltage input of RTDs. All the testings are conducted in still air at room temperature.

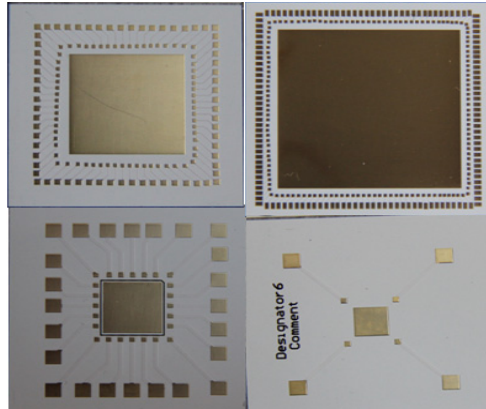


Figure 3.9: Various heat spreaders according to the size of test chips.

Resistance temperature detectors (RTDs)

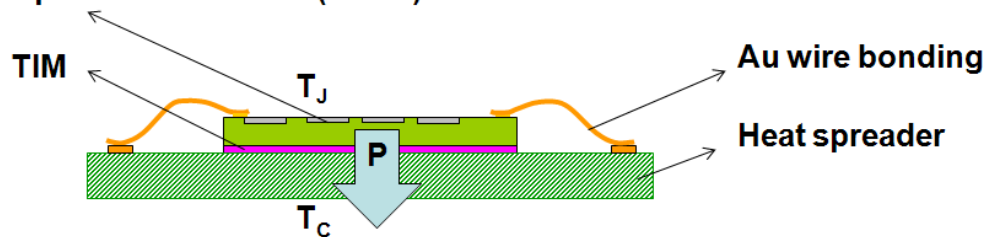


Figure 3.10: Illustration of the thermal dissipation testing system.

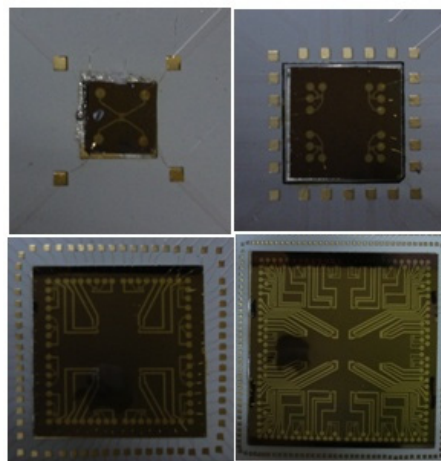


Figure 3.11: Packaged thermal dissipation testing systems assembled with different sized chips and TIMs: 5×5 , 10×10 , 20×20 and 30×30 mm².

Figure 3.12 gives the T_J testing results detected by the RTDs under different input powers. The T_J of the PI fiber-indium composite-based TIM is lower than that of thermal grease in each power loading, and the difference is increased linearly with increasing power loading. Figure 3.12 also shows the influence of the dimension of the composite-based TIMs on the T_J . The lowest junction temperature appears on the $30 \times 30 \text{ mm}^2$ sample in each power level and the difference increases with the power level.

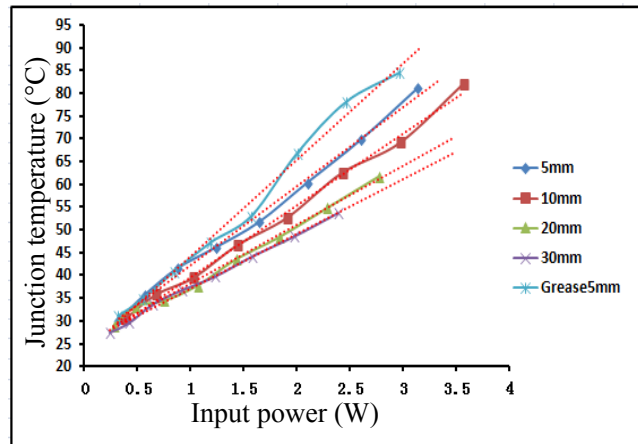


Figure 3.12: T_J variation detected by thermal dissipation testing systems under different input powers.

R_{thJC} of the heat dissipation testing system is calculated and the average value at different power levels is shown in Figure 3.13. The $5 \times 5 \text{ mm}^2$ sized packaging system decrease 50% in R_{thJC} when the TIMs changed from commercial thermal grease to the PI fibers-indium composite-based TIM. It is shown that the larger area of the PI fibers-indium composite-based TIM used, the lower the R_{thJC} of the packaged system is observed.

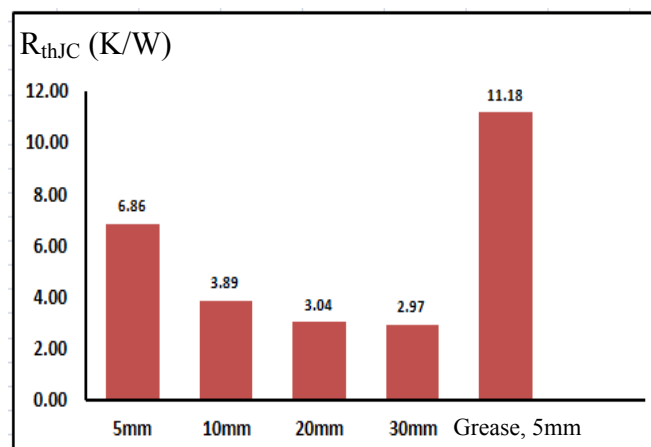


Figure 3.11: Average R_{thJC} from the thermal dissipation testing systems with different sized chips and PI fiber-indium composite TIMs: 5×5 , 10×10 , 20×20 and $30 \times 30 \text{ mm}^2$, and the reference packaged system with $5 \times 5 \text{ mm}^2$ sized chip and thermal grease TIM.

3.2.3 Thermal reliability tests

In order to evaluate the long-term reliability of the polymer fiber metal matrix composite, thermal cycling test from -40 to 115°C at a heating/cooling rate of $5^{\circ}\text{C}/\text{min}$ is carried out. The changes in thermal resistance of the PI fiber-indium composite and pure indium sample are presented after different cycles in Figure 3.12. The overall trend is that the thermal performance of the PI fiber-indium composite is found to be more stable than the pure indium TIM. On average, the PI fiber-indium composite samples increase by 10% while the indium samples increase by roughly 25%. This indicates that the PI fiber-indium composite can provide good reliability comparing to the pure indium TIM.

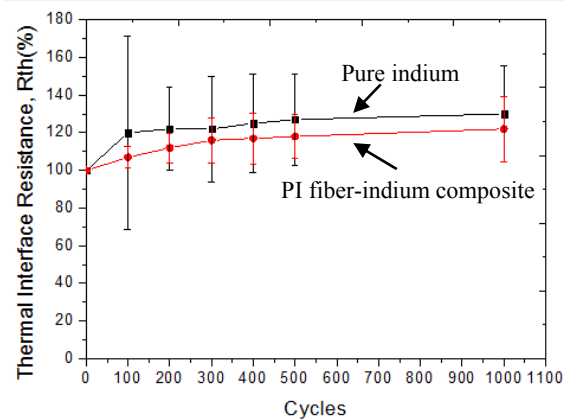


Figure 3.12: Variation of thermal resistance of the PI fiber-indium composite during thermal cycling test in comparison with pure indium sample.

The changes in thermal resistance of the PI fiber-SnAgCu composite sample are presented in Figure 3.13. After 1000 cycles, the thermal resistance of the PI fiber-SnAgCu composite is found to be largely unaffected, which indicate that the joints are kept reasonably intact through the thermal cycling. Most of the samples stayed within 20% of the initial resistance. Only one sample shows an increase in the range of 20-40%.

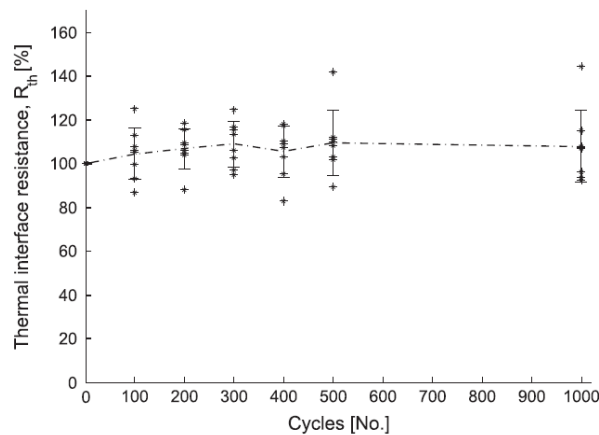


Figure 3.13: Variation of thermal resistance of the PI fiber-SnAgCu composite during thermal cycling test.

3.3 Mechanical properties of polymer fiber metal matrix composite-based TIM

3.3.1 Shear tests of PI fiber-InSnBi and PI fiber-indium composite

PI fiber-InSnBi composites with different thicknesses (50 μm , 70 μm and 100 μm) are reflowed at 70 $^{\circ}\text{C}$ for 3 min in air between two PCBs with an Sn coating under the a pressure of 1, 2, 3, 4, 5 and 10 Psi, respectively. The shear speed is 2 mm/s. Shear strength can be obtained from the ratio of maximum shear force and the size of TIM. As shown in Figure 3.14, the shear strength of the 70 μm and 100 μm samples show a similar trend and exceed the strength of the 50 μm thick samples. From 1 Psi to 4 Psi, the shear strength increases slightly along with increasing pressure, while from 4 Psi to 10 Psi, the shear strength begins to decline.

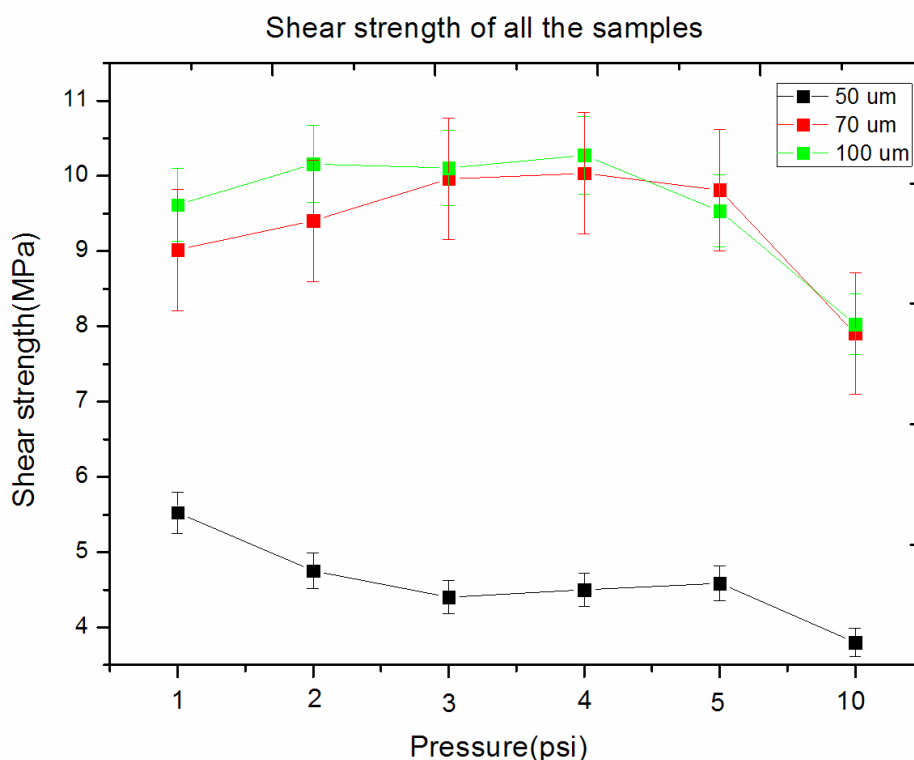


Figure 3.14: Shear strength of PI fiber-InSnBi composites with different thicknesses and reflow pressures.

The samples with 50 μm thickness soldered under pressure of 1 Psi and 10 Psi are shown in Figure 3.15a and b, respectively. The sample with higher shear strength shows almost no overflow of the InSnBi alloy, while the overflow has occurred in the samples with lower strength. The shear strength of the composite is attributed to the solders wetting with the mating surfaces. It is expected that the thicker TIM contains more metal so it retains higher shear strength even at higher reflow pressure.

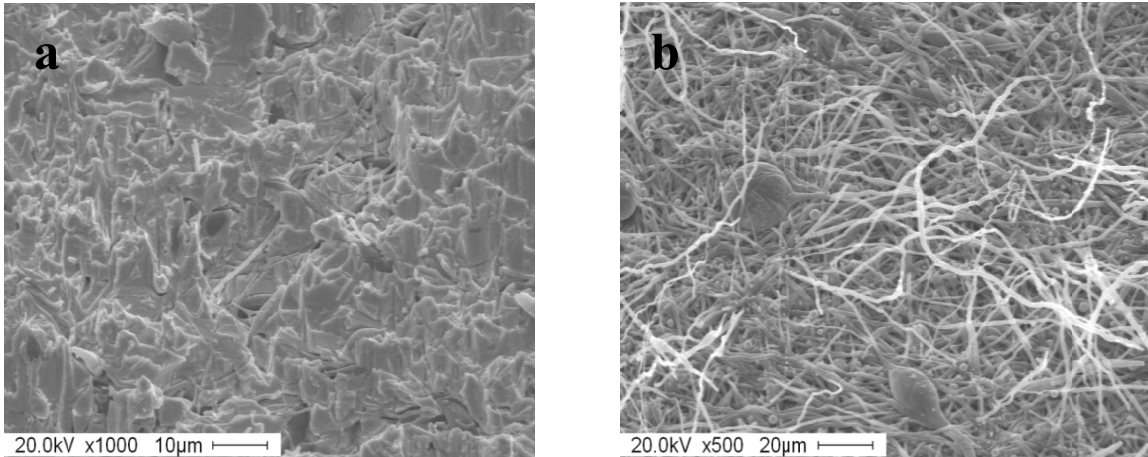


Figure 3.15: Shear fracture of 50 µm thick PI fiber-InSnBi composite samples reflowed at a pressure of 1 Psi (a) and 10 Psi (b).

To investigate the thermomechanical reliability of the PI fiber-InSnBi composite, a heat-humidity test is conducted in conditions of 40 °C and 93 % Relative Humidity (RH) for 0, 2, 4, 10, 21 and 56 days, respectively. The shear strength of the composite does not vary largely as shown in Figure 3.16. The shear strength decreases slightly at first after the thermal and humidity test for 2 and 4 days and then increases a little after the thermal and humidity tests over a longer period time. The bonding between the InSnBi alloy and Sn coating layer is affected by the penetration of the moisture at first and then enhanced by the diffusion of the metal at such temperature.

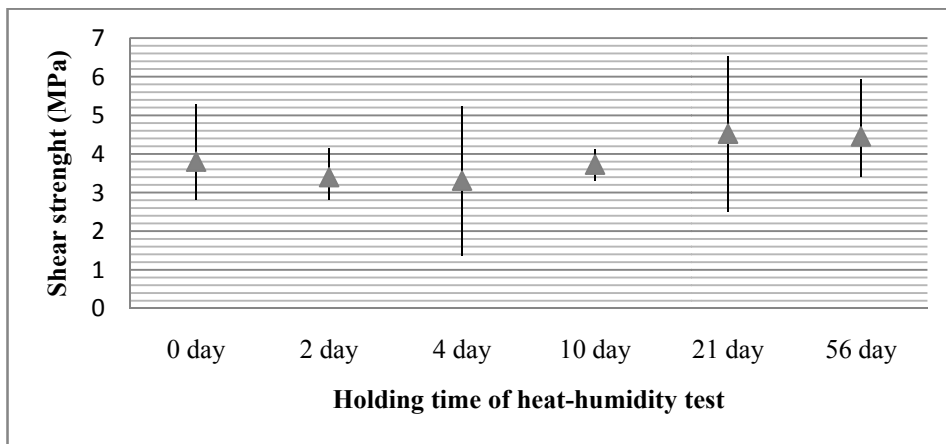


Figure 3.16: Shear strength variation of PI fiber-InSnBi composite after heat-humidity tests.

The shear tests of PI fiber-indium composite are also carried out by sandwiching them between PCBs with an ENIG layer, Cu and Sn coating, respectively. As shown in Figure 3.17, the shear strength of the bonding interface between the TIM and the Sn metal can reach as high as 4 MPa and is the highest among the three types of pads.

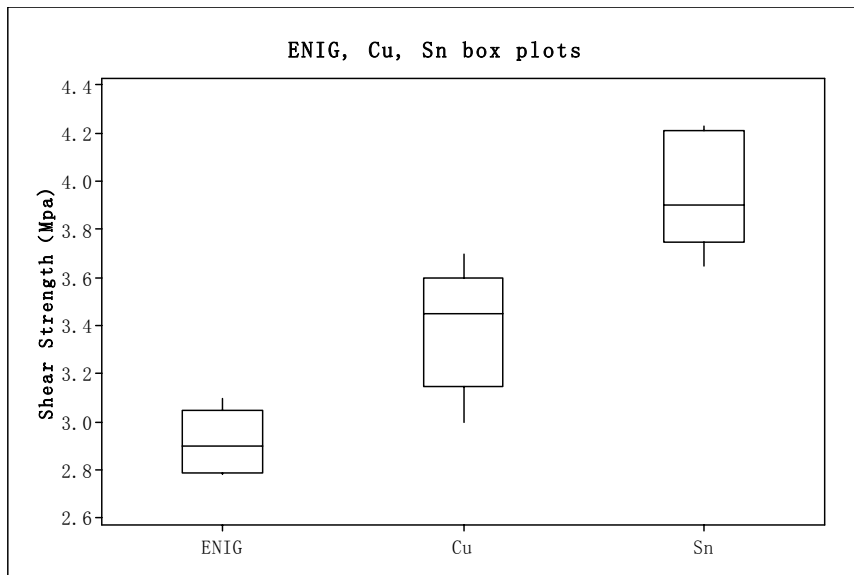


Figure 3.17: Shear strengths of the PI fiber-indium composite with different mating surfaces.

Also, the mechanical reliability of the samples is tested in the 85°C and 85RH environments based on GB/T2423.3-2001 [82]. Figure 3.18 shows slight variations in the shear strength of the composites with different holding times in the 85/85 environments, indicating the great moisture/oxidation resistance of such materials. Generally, the Sn and Cu coating is sensitive to the oxidation or corrosion in the heat and damp conditions, the good wettability of the indium matrix renders the close coverage on the mating surfaces, and then guarantees the consistence of the shear strength.

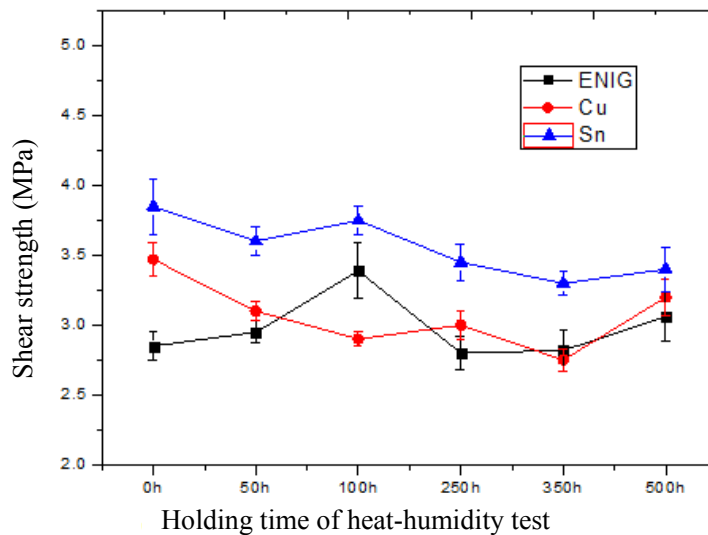


Figure 3.18: Shear strength variation of PI fiber-indium composite after 85/85 heat-humidity tests.

3.3.2 Tensile test of PI fiber-indium composite

The tensile properties of PI fiber-indium composite-based TIM are investigated at different temperatures and strain rates. The tests are conducted at 20, 50 and 80 °C (0.68, 0.75 and 0.82 T_m), respectively, which are typically applied temperatures for TIMs in-field. Pure indium samples are also tested for inference.

Figure 3.19 shows the engineering stress-strain curves of the composite and pure indium tested at various temperatures with a strain rate of $1 \times 10^{-4} \text{ s}^{-1}$. The stress initially increases nearly proportionally with the strain. As the strain further increases, the slopes of all the composites' curves begin to fall. On the other hand, all the curves from the pure indium samples show a turnaround due to the stress saturation and necking [68]. However, the turnaround in the composite's curve at the stress maximum corresponds to the initiation of macroscopic crack of the composite from its one edge. The stress then reduces with the propagation of the crack.

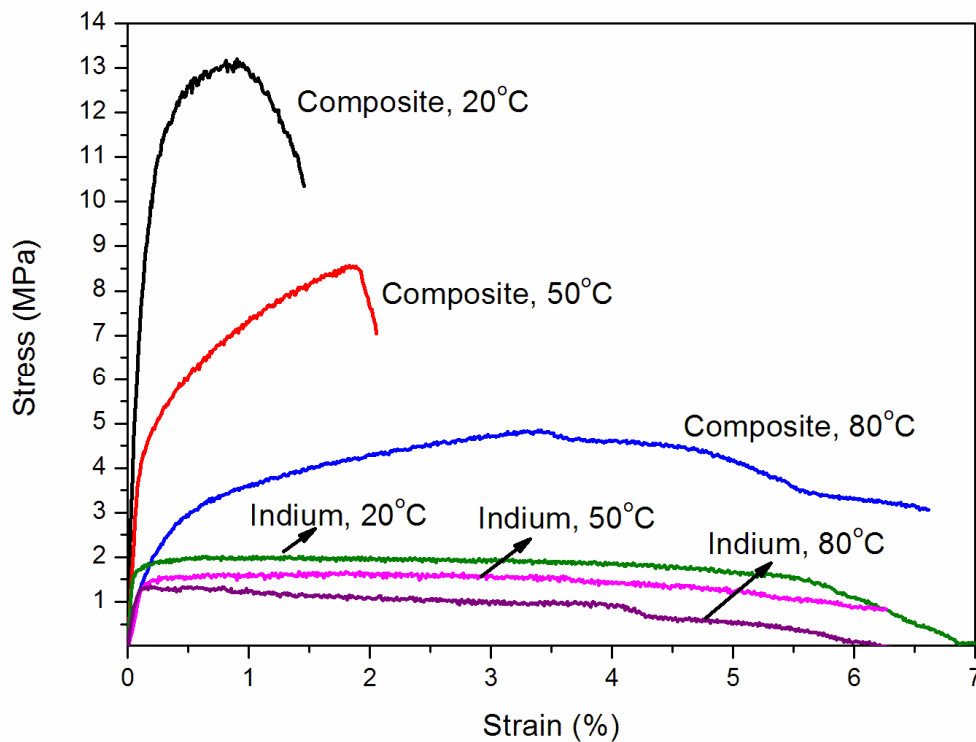


Figure 3.19: Engineering stress-strain curves of PI fiber-indium composite and pure indium at various temperatures with a strain rate of $1 \times 10^{-4} \text{ s}^{-1}$.

Since the effect of temperature is considerable, table 3.2 summarizes the averaged parameters including yield strength, UTS, tensile modulus and elongation at fracture. The yield strength is the tensile strength at a strain of 0.2%, which is decreased with increasing temperature for both the composite and indium. At 20 °C, the UTS of the composite is 5 times greater than that of pure indium. Evaluation of the Ag-coated fiber network without indium shows a tensile strength of less than 3 MPa (already considering real area of the cross section). The deterioration in strength is caused by the chemical treatment which is also reported by [83]. Therefore, the strength of the composite exceeds the summation of the strengths from

both the fiber network and indium by weight ration. The tensile modulus is calculated at a strain of 0.02% rather than 0.2% as normal, because of the relatively small elastic part during the deformation. This is the reason that the theoretical value of Young's modulus of indium (12 GPa) at room temperature is usually measured via a non-destructive method [84] other than tensile testing. Therefore, the value of the calculated modulus herein is lesser [69]. The elongation at fracture for composite samples is the strain at the maximum stress. For indium samples, the elongation at fracture is determined empirically owing to the wide necking range. It is noted that the elongation of indium is much less than the reported value [68, 69]. This is due to the fact that our tensile samples is in the form of film and the threshold of the crack initiation is lower than that of the rod samples used in other refs..

Table 3.2: Engineering yield strength, UTS, tensile modulus, elongation at fracture of PI fiber-indium composites and pure indium samples.

Sample	Yield strength (MPa)	UTS (MPa)	Tensile modulus (GPa)	Elongation at fracture (%)
Composite, 20°C	10_{-3}^{+2}	$13_{-0.2}^{+0.8}$	$10.6_{-1.5}^{+1}$	$0.9_{-0.1}^{+1.2}$
Composite, 50°C	$4.5_{-1.3}^{+0.8}$	8.6_{-2}^{+1}	$4.5_{-0.65}^{+0.4}$	$1.9_{-0.1}^{+0.9}$
Composite, 80°C	$1.5_{-0.3}^{+0.1}$	$5.9_{-1.9}^{+0.8}$	$2.0_{-0.15}^{+0.05}$	$3.6_{-0.2}^{+2}$
Indium, 20°C	$1.8_{-0.4}^{+0.2}$	$1.9_{-0.3}^{+0.4}$	$4.3_{-0.2}^{+0.1}$	>5
Indium, 50°C	$1.4_{-0.1}^{+0.08}$	$1.6_{-0.3}^{+0.1}$	$1.8_{-0.05}^{+0.04}$	>6
Indium, 80°C	$1.3_{-0.3}^{+0.03}$	$1.3_{-0.3}^{+0.08}$	$0.7_{-0.02}^{+0.02}$	>4

Figure 3.20 shows the effect of strain rate on the UTS of the composite at 20 °C. In spite of specimen-to-specimen variation, a clear trend can be seen that the UTS of the composite is inversely proportional to logarithmic strain rate in the range from $5e^{-5}$ to $5e^{-2} s^{-1}$. For most metallic materials, the UTS increases with increased strain rate [85, 86]. The contrary indicates that the introduction of a fiber network and the resulting interaction with indium exhibit new strengthening mechanisms for the composite.

Figure 3.21 shows crack morphologies of the PI fiber-indium composites after tension. In all tests, the tensile cracks are found to propagate from one side of the sample to the other side. The morphologies of cracks from indium are similar, so only one tested at 20 °C is shown in Figure 3.21. At the crack tip of the indium, there is a yielding area resulting from the local stress concentration indicated by an arrow in Figure 3.21a. The crack from the indium sample propagates with the fracture and movement of the yielding area. With the introduction of fibers, the mechanism of crack growth is more complicated. In spite of the difficulty in concluding the effect of the 3D fiber network, it is believed that the arrangement of the network could change the propagation of cracks. As indicated by the arrows in Figure 3.21b, there are many fibers on the boundaries of the crack and the fibers indicated by black arrows change the direction of the crack. It is speculated that the crack is apt to occur at the fiber-indium interfaces and propagate along the interfaces. One of the most remarkable differences of cracks at different temperatures

is that the structures of composites become looser after tension at higher temperatures. In Figure 3.21d, debonding from fibers and indium almost occurs in the whole sample and not only along the tensile crack, which results in largest elongation (Figure 3.19). In addition, the number of breakages of fibers (as marked by circles in Figure 3.21b) is counted from Figure 3.21 excluding the cracked parts. There are about 60, 30 and 20 breakages of fibers visible from Figure 3.21b, c and d, respectively. These counts indicate tensile stress loading levels along the fibers. At 20 °C, fibers play an important role in enduring the high tensile stress of the composite until the fibers break. At higher temperatures, debonding at the fiber-indium interface occurs before the fibers reach to their breaking point.

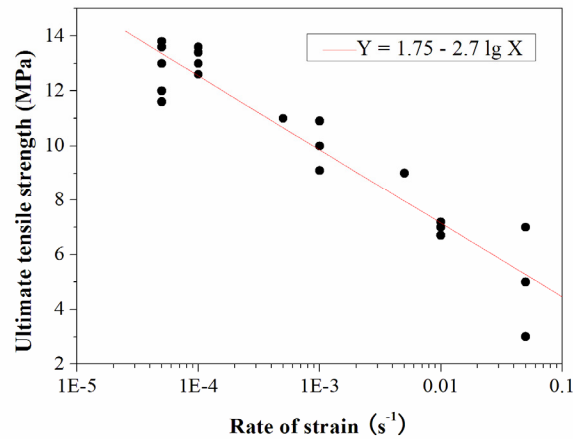


Figure 3.20: UTS variation with strain rate of PI fiber-indium composite at 20 °C.

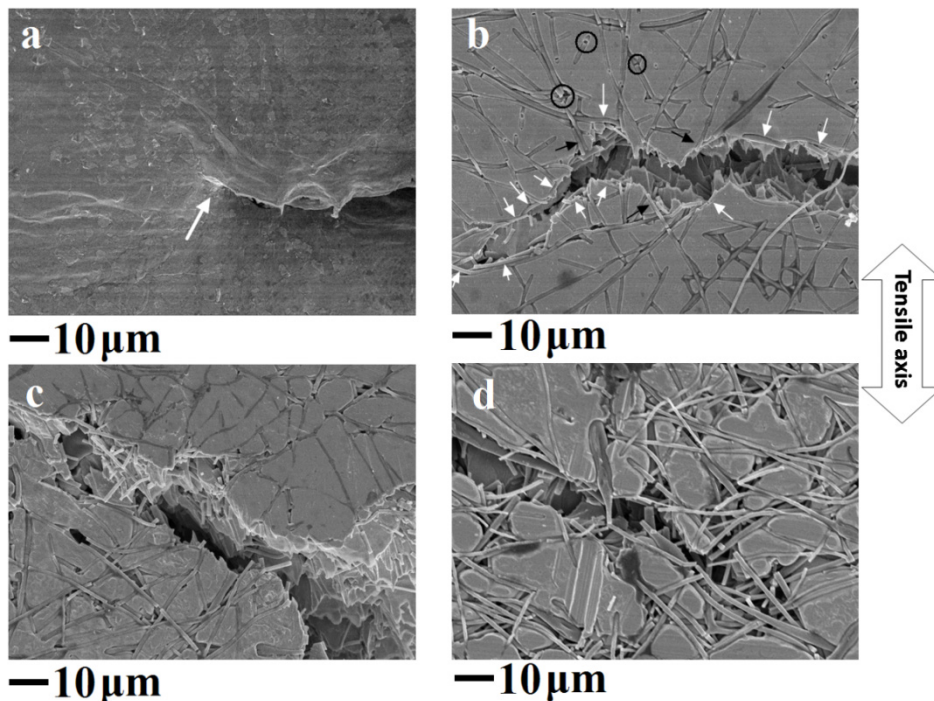


Figure 3.21: SEM morphologies of tensile cracks of indium tested at 20 °C (a) and PI fiber-indium composites tested at 20 (b), 50 (c) and 80 °C (d).

The effects of the fiber on the novel composite are further analyzed via fracture morphologies in Figure 3.22. The fracture of indium is dominated by ductile fracture in shear modes. Moreover, the indium necks to an edge, as shown by arrows in Figure 3.22a, and the reduction in area is close to 100%. In the composite, broken fibers and black holes resulting from the fibers' pulling out are detected. The smooth surface of the fibers indicates that the Ag coating shown in Figure 3.2c has been consumed and resulted in an AgIn_2 IMC that attaches to the indium matrix.

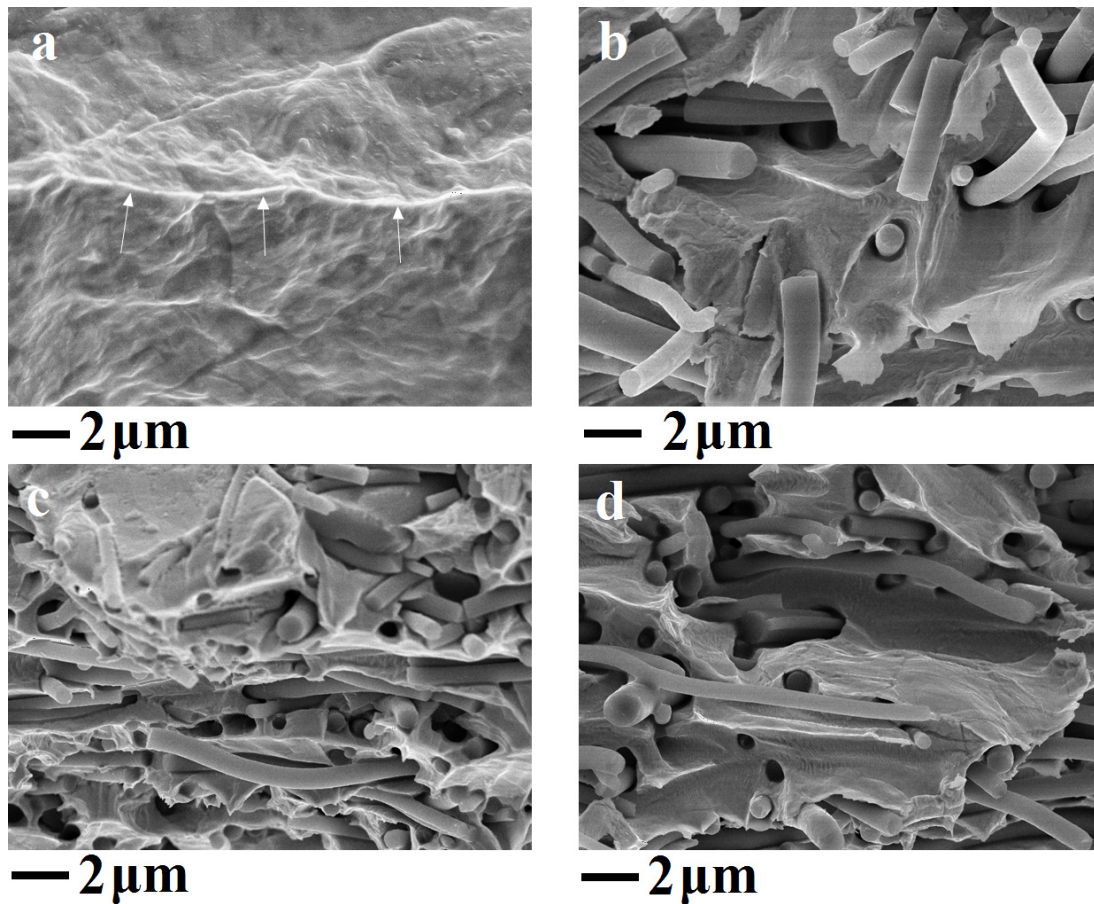


Figure 3.22: SEM fracture morphologies of indium after tensile tested at 20 °C (a) and PI fiber-indium composite tested at 20 (b), 50 (c) and 80 °C (d)

Figure 3.23 shows XRD patterns of the PI fiber-indium composites after tensile tests at various temperatures. The extraordinarily strong peak of (112) from the sample tested at 20°C indicates the existence of the preferred orientation of the indium resulting from the severe stress in the tensile test. With the rise in temperature, the lattice orientation of the composite normalizes and other diffraction peaks are more obvious due to the recrystallization of indium. Considering the position of the (101) peaks, the interplanar spacings of the planes from samples tested at 20, 50 and 80 °C is calculated by Bragg's Law to obtain to be 2.653, 2.691 and 2.715 Å, respectively. The interplanar spacing of (101) plane from standard indium is 2.715 Å, indicating that large lattice deformation or compression of indium exists in the sample of the composite tested at 20 °C other than the sample tested at 80 °C.

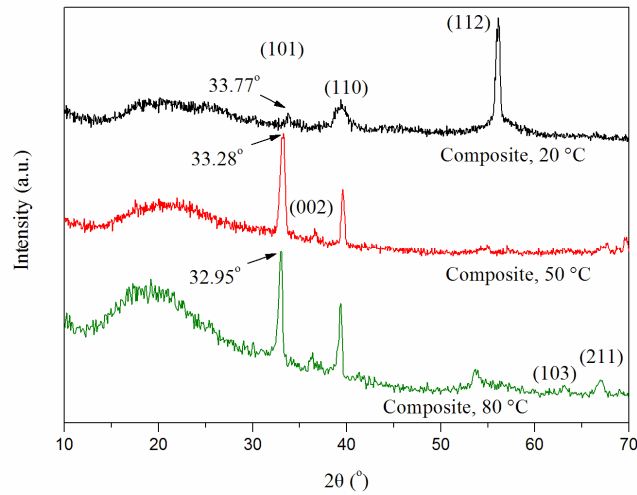


Figure 3.23: XRD patterns of PI fiber-indium composites after tensile tests at 20, 50 and 80 °C. All the diffraction peaks derive from indium.

In-situ TEM straining is an essential technique for observing deformation evolution of the composite at the nanoscale in real time. The samples used for the in-situ TEM testing are fabricated as shown in Figure 3.4 with 15 μm length and 5 μm width. Figure 3.25 shows breaking processes for the PI fiber-indium laminate. As expected, a tensile crack originates from one of the notches of the indium. The crack propagates perpendicular to the tensile direction and is arrested at the fiber-indium interface after 150 s (Figure 3.24e). Instead of peeling of the interface, the fiber breaks elsewhere to release the tensile stress (Figure 3.24f), indicating a solid bonding between the fiber and indium.

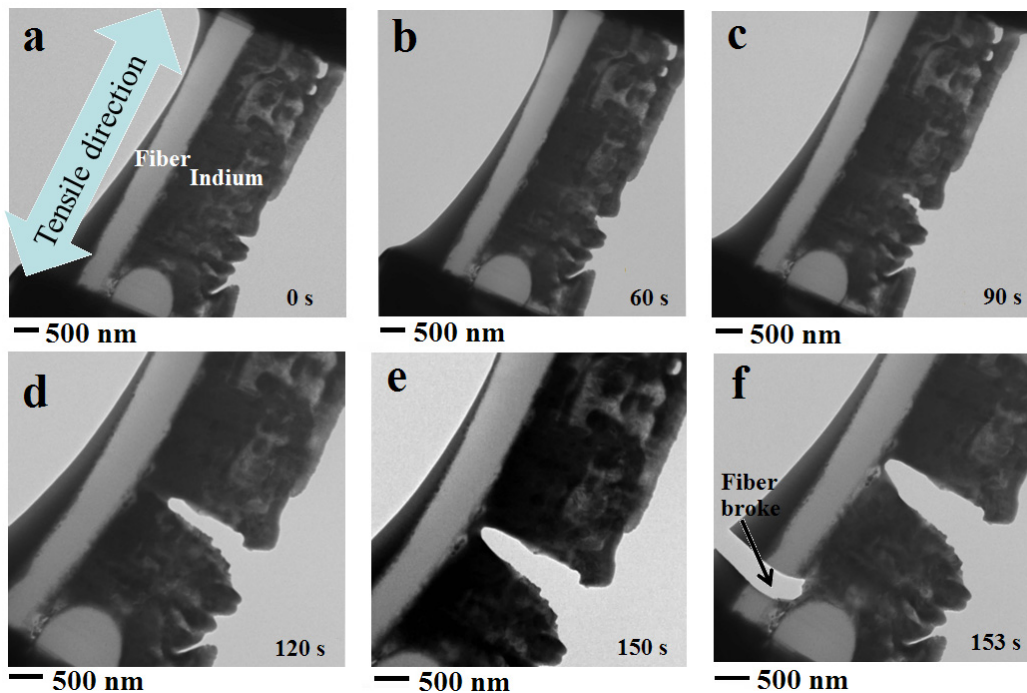


Figure 3.24: In-situ TEM straining images of PI fiber-indium composite laminate under tension after 0 (a), 60 (b), 90 (c), 120 (d), 150 (e) and 153 (f) seconds.

Figure 3.25 shows another in-situ TEM tensile test and the sample contains three cross sections of fibers. This sample is prepared to investigate the deformation behaviour of the composite when the tensile direction is perpendicular to the fibers. The indium in this sample consists of two grains and the grain boundary (GB) is indicated by black arrows in Figure 3.25a. Under tension, the indium deforms via the slipping of dislocation. There is a plastic deformed area consisting of slip lines and dislocations at the front of the crack (Figure 3.25b). As the crack grows, the area becomes larger and moves. Increasing slip lines also appear with the propagation of the tensile crack (Figure 3.25b, c and d). Figure 3.25e shows the slip lines are arrested by the GB and the fiber-indium interface. The restriction of slip in indium can reinforce the tensile strength of the composite and affect its elongation. The stress field of dislocation pileups at GBs could deform the next grain easily because of the low strength of indium and its various slip systems including (111), (101) and (001) planes [87, 88]. However, fiber-indium interfaces are stronger obstacles for dislocation motion due to the hard IMC layers and the large diameter of the fiber. Therefore, the fibers could strengthen the composite by themselves, IMC bonding (Figure 3.24) and the obstructive interfaces (Figure 3.25). Figure 3.25f shows the details on the crack tip. In the front of the crack, there is a dislocation-free zone (DFZ) which has been detected by many metals [89]. There are dislocation emission, proliferation and movement at the crack tip. Consequently, two dislocation arrays on both sides of the DFZ slip to the GB. Although there are various slipping directions in indium, it is believed that the two location arrays both slip perpendicularly to the tensile direction. They are not parallel because of the distortion of the sample in which stress is relieved by cracking on only one side of the sample. Due to the fact that only (011) plane could be the composition plane of twins in indium [90], we believe the sole annealing twin grows along the (011) plane and the movement direction of the dislocation arrays is $[\bar{1}\bar{1}0]$. Furthermore, according to the intersection angle between the dislocation arrays and the slip lines, the crossed slip lines are expected to be divided into (011) and $(10\bar{1})$ groups.

From the results of tensile tests and in-situ TEM straining observation, a strengthening mechanism is presented in Figure 3.26. To simplify the situation, we assume a small area, which contains indium, two continuous fibers (grey) and IMC layer (black) as illustrated in Figure 3.26. When fibers are almost parallel to the tensile direction (Figure 3.26a), the tensile strengths of fibers (σ_{fiber}) and IMC (σ_{IMC}) contribute most of the tensile strength of the composite, while the strength of indium accounts for a small part. Figure 3.26d shows a practical example in such a condition when two fibers are embedded in indium matrix. The indium around them shows a sign of large stretching along the tensile direction. Most of fiber-reinforced composites have been designed by this strengthening mechanism [91]. However, the fibers with such orientation only account for a small proportion. In the second case, when fibers are nearly perpendicular to the tensile direction (Figures 3.26b and e), the tensile strength of the composite should be identical to the strength of indium (σ_{indium}) because σ_{indium} is less than the bonding strength at interface, as Figure 3.24 indicates. However, cracks often occur at fiber-indium interfaces, as shown in Figure 3.26e, because dislocations of indium slip to the interfaces, as Figure 3.25 displays, making the interfacial parts susceptible to cracking. Figures 3.26c and f present the most common case in which two fibers intersect at a certain angle. The two fibers under tension would be rearranged to the tensile direction if without the existence of indium. With the infiltration of indium, the two fibers compress the indium in the upper and lower part in Figure 3.26c. The compression makes the indium deform and enhances the bonding strength at the interfaces. The bonding strength can be represented as

shear force at the fiber-indium interface. The stronger compression provides the larger bonding strength, and thus the higher tensile strength of the composite.

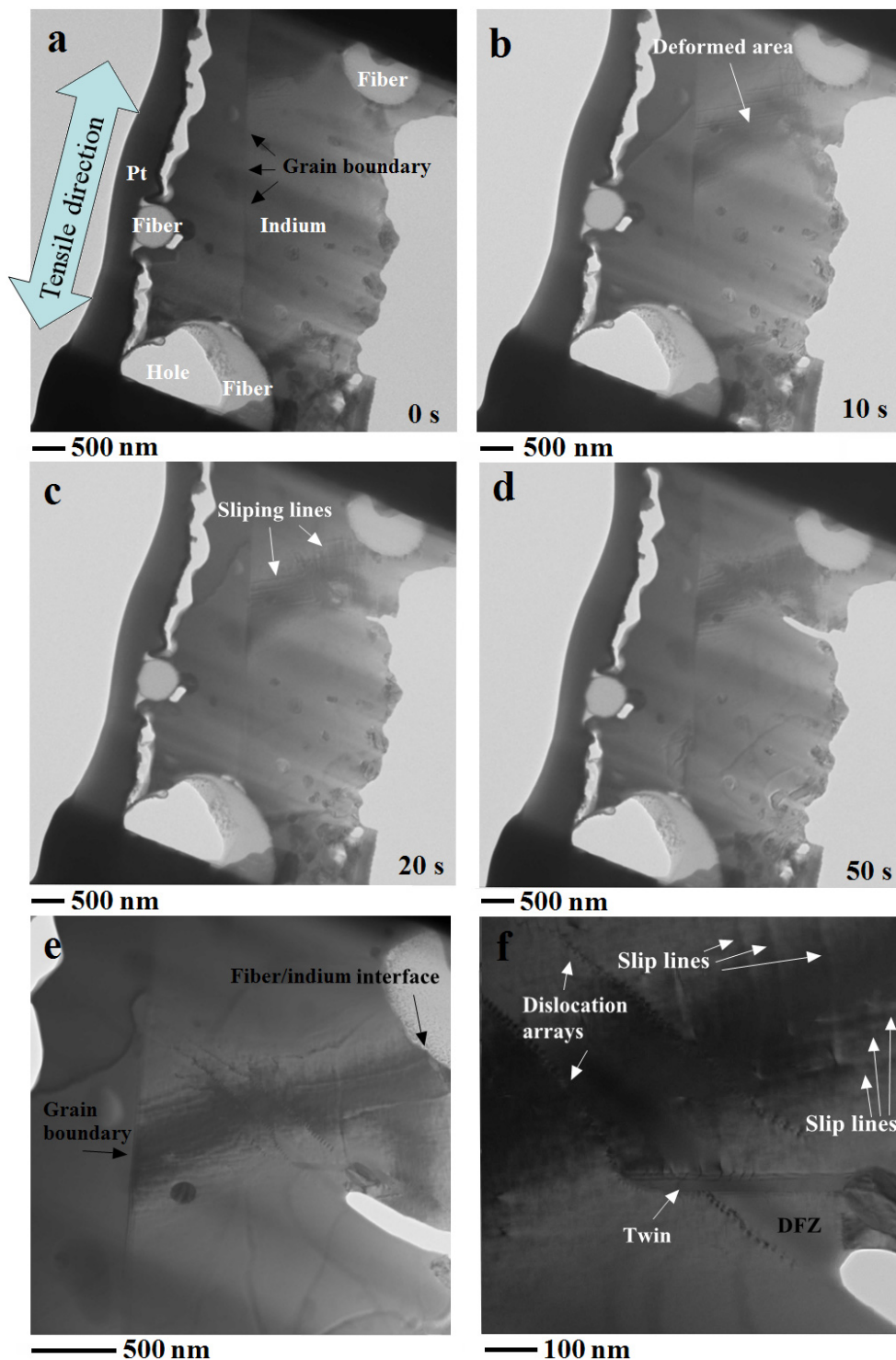


Figure 3.25: In-situ TEM straining images of a PI fiber-indium composite laminate under tension after 0 (a), 10 (b), 20 (c) and 50 (d) seconds; (e) is the TEM image of arrested slip lines by GB and a fiber-indium interface; (f) is TEM morphology on the crack tip and the DFZ indicates a dislocation-free zone.

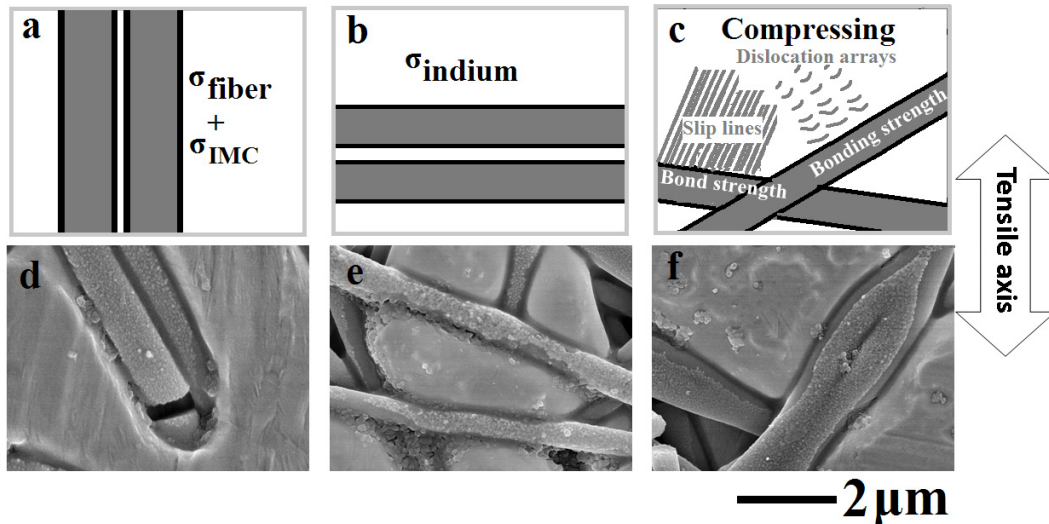


Figure 3.26: Illustration of strengthening mechanisms of PI fiber-indium composite when two fibers are almost parallel (a) or perpendicular (b) to tensile direction or intersect each other (c); the grey parts in (a, b, and c) denote fibers and black parts denote IMC layers; SEM photos (d, e and f) correspond to the three typical conditions.

It is noted that there are numerous random-orientation fibers, and even the left and right parts of indium in Figure 3.26c are compressed by other fibers. The indium part and its surrounding fibers could form a solid mutually reinforcing structure to give enhanced tensile strength. The compression at the interfaces could protect the integrity of fibers and the fiber networks serve the composite structure in turn. At 80 °C, the tensile strength of the composite is lower than that at 20 °C because the planar slip of indium becomes easier, and then the compressed parts in Figure 3.26c deform resulting in the debonding with fibers. The mutually reinforcing structure could not form, so the tensile strength of the composite decreases, as shown in Figure 3.19 and table 3.2. The mutually reinforcing structures in the tensile sample at 20 °C have suffered more compression showing more breakages of the fibers in Figure 3.21 and severer lattice distortion of indium in Figure 3.23.

The strengthening mechanism based on the mutually reinforcing structure could also be used to explain the impact of strain rate. The lower rate of strain gives indium enough time for recrystallization and deformation [69] to adjust for conformable contact with fibers, thus keeping larger compression and bonding strength. The dislocation movement is fundamental for the effect of the compression, as shown in Figure 3.25. It is known that the pileups of dislocation give rise to a stress field nearby, which increases the compression at the interfaces, as shown in Figures 3.25e and 3.26c. The ends of slip lines at interface could bring out dislocations too. With more time for the microstructural adjustment, the solid mutually reinforcing structure provides enhanced tensile strength. The compression could reach its limit when the mutually reinforcing structure collapses due to the breakage of fibers or fracture of indium, then the tensile strength maximum of the composite is detected as shown in Figure 3.19. It is noted that the strengthening mechanism is used to interpret the tensile behaviour of the composite before its macroscopic fracture. When the tensile stress reaches its maximum, the mutually reinforcing structure is destroyed and the failure of the composite is like Figure 3.21: a macroscopic crack initializes on indium and grows to the fiber-indium interface, then the crack propagates along the fiber-indium interfaces.

3.3.3 Creep tests of PI fiber-indium composite

Creep tests of the PI fiber-indium composite have been conducted via a standard mechanical testing machine (5548 Micro Tester, Instron) at 20 °C (0.68 T_m of indium). The specimens are cut from castings in a dumbbell shape with a rectangle cross section of $5 \times 0.05 \text{ mm}^2$ and gauge length of 20 mm. Figure 3.27 shows the creep curves of both the composites and pure indium samples at various stresses after eliminating the initial strain. The strain curve of the indium tested under 0.2 MPa typically shows the three creep stages: primary, secondary (steady state), and tertiary (necking to failure). However, due to the large scale of the axes in Figure 3.27, the indium under 1 MPa and the composite under 2 MPa show almost straight lines, indicating extreme low and high creep resistance, respectively. Regarding the composite at 5 MPa, the curve shows no typical creep stages but rather an ascending strain curve with terraces. The slope of the composite under 5 MPa shows a low creep rate of 1.54×10^{-7} , and the creep rupture time is orders of magnitude longer compared to pure indium. Table 3.3 summarizes the averaged steady creep rate and creep rupture life of the tested samples. Compared to indium samples, the composites exhibit a very low steady creep rate and long creep rupture life.

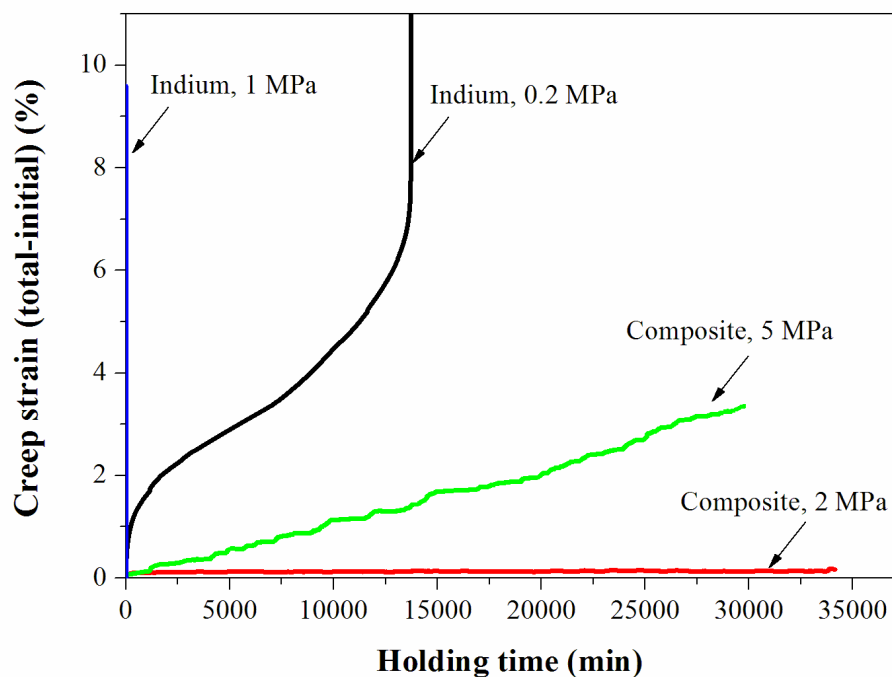


Figure 3.27: Creep stages of PI fiber-indium composite and pure indium at room temperature and different stress levels.

The creep curve from the composite at 5 MPa is analyzed in combination with in-situ TEM straining and SEM observation, as shown by Figure 3.28. Starting with a steep upward curve, the initial part of the creep curve is relative to the elastic deformation of the composite, as shown by Figure 3.28a. The creep strain increases slowly, resulting from the propagation of a crack growing within the indium parts (Figure 3.28b). After the crack extends at the

fiber-indium interface, the fibers start to break and the breakage of the fibers corresponds to the sudden increase in strain, showing the steps in the curve. The processes shown in Figures 3.28a-c occur repeatedly resulting in numerous steps and terraces in the creep curve. The fibers, which are in parallel with the stress axis, break first because they carry the loading stress mainly. After breakage of these fibers, other fibers bear the stress and fracture in succession according to the angle at which they intersect with the stress axis. Besides the microscale cracks of indium, the planar slip of indium is also responsible for the ‘smooth’ increased strain, as shown by Figures 3.28d and e. With more holding time, the indium part shows more slip lines. As mentioned before, Figures 3.28d and e show that the slip lines are hindered by the indium’s GB and the fiber-indium interfaces. Therefore, the restriction of indium slip reinforces the composite’s strength and improves its creep resistance. With enough applied stress and holding time, the composite approaches the creep fracture with broken fibers and necking indium (Figure 3.28f).

Table 3.3: Steady creep rate and creep rupture life of PI fiber-indium composites and pure indiums at various stresses.

Sample	Steady creep rate (s^{-1})	Creep rupture life (min)
Indium, 0.2 MPa	4.65E-5	≈ 14000
Indium, 1 MPa	1.74E-3	≈ 18
Indium, 2 MPa	1.6E-2	≈ 8
Composite, 1 MPa	≈ 0	> 34000
Composite, 2 MPa	≈ 0	> 34000
Composite, 5 MPa	1.54E-7	> 30000

Due to the low strength [68] and various slip systems [87], the creep threshold of pure indium is quite low. With the introduction of the PI fibers, the creep threshold of the composite is increased to become the fracture strength of the PI fiber. If the applied stress is low enough not to induce breaking the fibers, creep does not seem to occur. This appears to be the situation for the composite with an applied stress of 2 MPa in Figure 3.27. According to the results, the fibers in the composites show a quite low UTS, The deterioration of the PI’s strength is due to the negative effects of the Ag-coating chemical treatment [83]. If the chemical treatment can be adjusted to limit the damage of the PI fiber, it is possible that the mechanical properties of the composite could be improved even further.

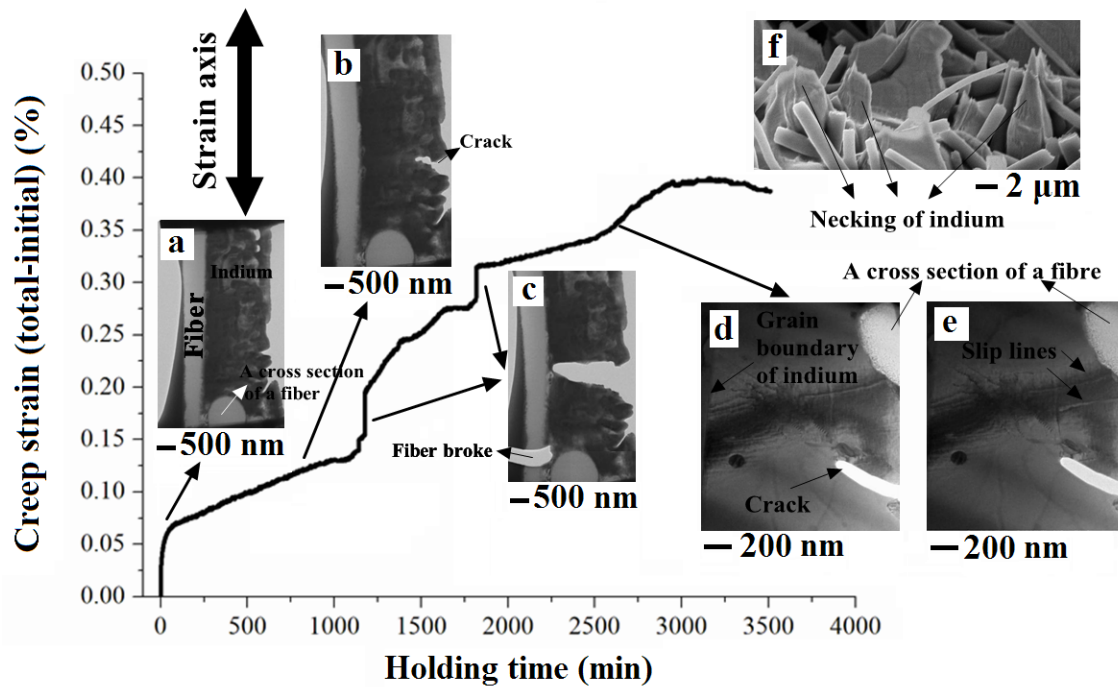


Figure 3.28: Creep curve of PI fiber-indium composite at 5 MPa in combination with in-situ TEM images (a)-(e) under tension and SEM image showing creep fracture of the composite (f).

3.4 Summary and Discussion

With the composite design of fiber network and infiltrated metal, three types of novel TIMs are prepared and characterized for their thermal performances and mechanical properties. The novel polymer fiber metal matrix composite-based TIMs consist of 3D porous randomly oriented continuous PI fibers and infiltrated metal/alloy. Solid bonding between the fiber and metal matrix is achieved via the formation of a nanoscale AgIn_2 IMC layer or direct contact.

The PI fiber-indium composite as die attachment material has good thermal performance on chips for heat dissipation. The steady-state junction temperature and junction-to-case thermal resistance of heat dissipation testing systems packaged with the PI fiber-indium composite have been studied. The results show that the heat dissipation effect of the novel TIM is better to that of current commercial ones.

The PI fiber-InSnBi composite of 70 μm will be suitable for use as it offers better shear strength. If serious overflow of the alloys occurs during reflow, the shear strength will drop dramatically. The good reliability of the PI fiber-InSnBi composite is also confirmed through the heat-humidity aging measurements. Shear strength between the Sn surface and the PI fiber-indium composite can reach 4 MPa and is better than the strength with an ENIG and Cu coatings.

The PI fiber-indium composite exhibits the ultimate tensile strength five times greater than that of pure indium. With rising temperatures, the tensile strength decreases while the elongation at fracture increases. Tensile cracks propagate along the fiber-indium interfaces so the arrangement of fibers changes the direction of crack growth. In addition, the UTS of the composite is found to be inversely proportional to the logarithmic strain rate in a certain range.

In-situ TEM straining of the composite shows the tensile crack initiates from indium and propagates to fiber-indium interface, and then continues to grow after the breakage of fiber. Under tension, there is dislocation emission, proliferation and movement at the crack tip of the composite. Aside from the dislocation-free zone, dislocation arrays slip to GB or fiber-indium interfaces, and slip lines are also arrested by these obstacles. These obstacles affect the deformation of indium and strengthen the composite by forming solid mutually reinforcing structures in combination with indium matrix. The strengthening mechanism highlights the compression at fiber-indium interfaces, which conduces high shear force at the interfaces and thus improves the tensile strength of the composite. At a higher temperature, mutually reinforcing structures cannot form due to the easy-slip of indium. At a low strain rate, the composites have enough time to accommodate themselves to the mutually reinforcing structures by slip and/or recrystallization. The tensile strength reaches its maximum when fiber networks cannot endure the stress and the mutually reinforcing structures collapse.

A simple analytical model developed by Markaki and Clyne [92] is partially analogous to our case. They report that the modulus of composite is related to the modulus ratio of matrix and fiber. In this work, we have the added complexity that the modulus of indium could change due to the planar slip or strain hardening of indium, and the modulus of fiber could also be 'increased' with the positive effect of the compression. To establish an analytical model for further work in our case, first, the bonding strength at the indium/fiber interface should be quantized under various compression conditions, then the fibre network architecture should be extracted via X-ray tomography [93], and finally we should analyze the bonding strength distribution in the whole composite using the finite element method (FEM).

The PI fiber-indium composite also exhibits higher creep resistance: a lower steady creep rate and a longer creep rupture life comparing to pure indium. The steps in the composite's creep curve are due to the breakage of the PI fiber, and the creep threshold of the composite corresponds to the fiber's fracture strength. The fiber-indium interfaces can block the motion of the indium slip, resulting in the enhanced creep properties of the composite. In combination with earlier measured thermal properties, the observed effects on the mechanical properties show a large potential for the composite to fulfill the thermomechanical requirements in thermal management applications.

Chapter 4

Thermally conductive fiber metal matrix composite-based TIM

To further improve the thermal performance of the fiber network metal matrix composite-based TIMs, it is of considerable interest to update the polymer fibers with highly thermally conductive ones. This chapter presents another type of TIM consisting of thermally conductive nanofibers and a metal matrix. BN nanofibers and carbon fibers have been fabricated by electrospinning process and heat treatment. After surface metallization by sputtering, the porous fiber film is infiltrated with liquid metal by squeeze casting. Thermal conductivity tests of these new composites are introduced afterwards.

4.1 Boron nitride fiber-indium composite-based TIM

4.1.1 Composite fabrication

Hexagonal boron nitride (hBN) fiber is a promising alternative due to its high thermal conductivity and excellent thermal and chemical stability [94, 95]. The h-BN lattice consists of stacked layers with B-N atoms above one another with weak interlayer van der Waals bonds. The atoms in the a-b planes are bonded to their three nearest neighbors of a different species through strong covalent bonding of sp^2 hybridized orbital. BN fillers are the most cost-effective material with high thermal conductivity and electrical insulating properties among many current TIMs in use [23]. BN powders and BN nanotubes have been studied for thermal management in the electronic industries [39, 96-100], however, BN fibers have received very little attention as engineering materials.

BN fibers have been prepared for the first time in 1966 by the spinning and nitriding of melt-drawn boron oxide [101, 102]. Via the same technology, a series of melt-spinnable polymer precursors, such as poly(borazinylamine) [103], poly(borazine) [104] and Polyborazylene [105] are developed to produce BN fibers. However, the temperature and atmosphere need careful controlling in the melting spinning process. Another disadvantage of this process is that the diameter of the resultant BN fiber is very thick, ranging from 1 to 10 microns. Using the electrospinning setup, BN nanofibers have been prepared by Qiu's group [106, 107]. It is shown that electrospinning of the B_2O_3 precursor solution, followed by heat treatment in an NH_3/N_2 atmosphere is an effective and facile method to process BN nanofibers in volume production.

The boron oxide fiber network is fabricated by electrospinning B_2O_3 (boric anhydride, 99.98%, Sigma-Aldrich)/PVB (polyvinyl butyral, Sigma-Aldrich) dissolved in methanol. The nitriding process for the precursor is rapidly heating to 1000 °C in pure NH_3 for 2 h and then to 1500 °C in pure N_2 for 2 h. Afterwards, thin layers of titanium (120 nm) and gold (120 nm) are deposited by sputtering on the fibrous network to enhance wetting with metal. The BN film is infiltrated by liquid indium. The electrospun precursory fibers are displayed in Figure 4.1a. The mean diameter of the fibers is approx. 800 nm (std. dev. 400 nm). After the nitriding and annealing treatment, the integrity of fiber is retained (Figures 4.1b and c). Figure 4.1d shows the compact and uniform sputtering particles on the surfaces of fibers. The conversion from boron oxide to boron nitride is confirmed by attenuated total reflectance Fourier transform infrared spectroscopy (ATR-FTIR) and XRD. The FTIR spectra (Figure 4.2a) display the results from the fibers before and after the heat treatment. All the peaks from functional groups of boron oxide and PVB in the precursor fibers disappear, and hBN's peaks appear [106, 107]. Figure 4.2b shows the XRD pattern of the resultant BN fiber film, where two peaks are obviously observed. There is a broad peak around 25° corresponding the turbostratic structure of the boron nitride and overlaying (002) peaks of hexagonal structure at 26.3° [108]. The other relatively weak peak at 43° also demonstrated that the BN crystal is not completely hexagonal, showing the hexagonal structure with 2D order but 3D disorder [101, 109-112].

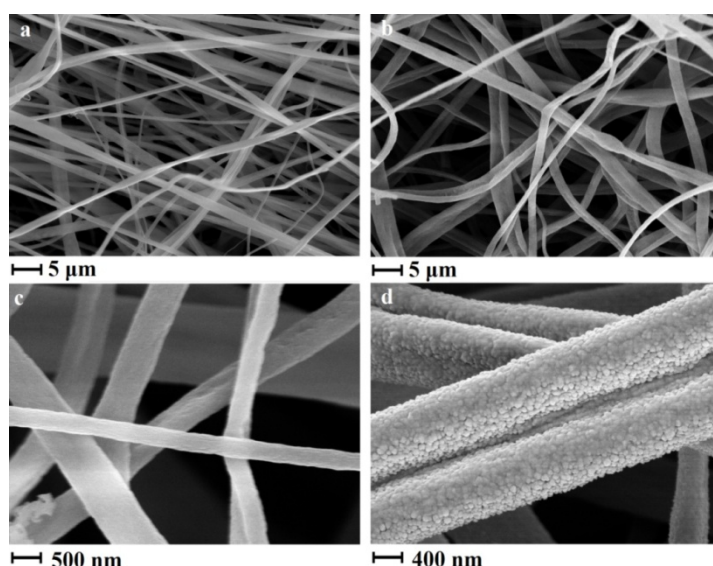


Figure 4.1: SEM images of precursory fibers (a), BN fibers (b, c) and sputtered BN fibers with Ti/Au layers (d).

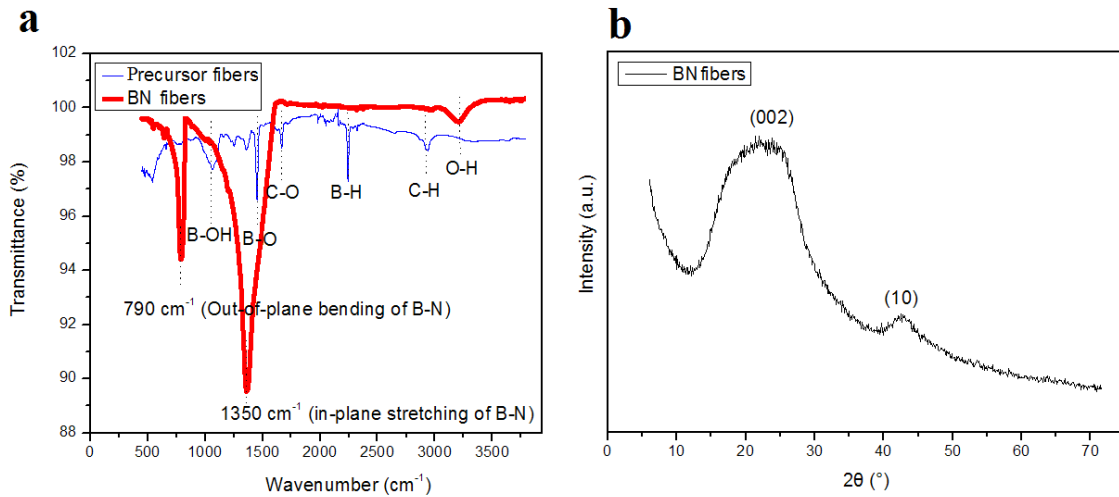


Figure 4.2: FTIR analysis (a) and XRD pattern (b) of the resulting BN fibers.

Figure 4.3a depicts the surface view of the final BN fiber-indium composite. Clearly, the indium alloy is infiltrated into the interspaces among the BN fibers. To investigate the inner filling of the film, a solution of 10 ml HF, 10 ml H₂O₂, and 40 ml H₂O is used to remove indium from the surface of the film. Figure 4.3b revealed the ‘inside’ structure of the composite after the etching. The Metal phase has almost filled the porous network showing good infiltration.

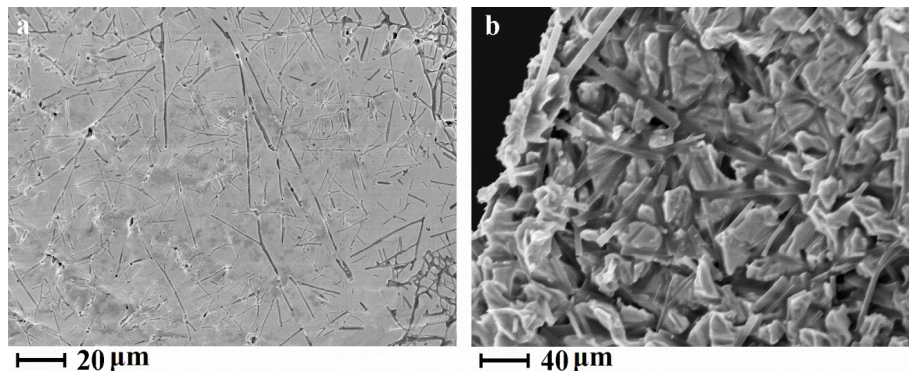


Figure 4.3: SEM images of BN fiber-indium composite-based TIM after infiltration (a) and the ‘inside’ structure after surface etching by diluting HF acid (b).

4.1.2 Characterization of thermal performance

The in-plane thermal conductivity of the BN fiber-indium composite has been obtained as mentioned in section 3.2. The density of the BN fiber-indium composite is 4.0 g/cm³ measured using the drainage method. Considering the density of pure indium (7.3 g/cm³) and hexagonal boron nitride (2.2 g/cm³), the composite consisted of 31.3% BN and 68.7% indium in weight. By considering the weight ratio, the specific heat of the composite is calculated to be 420 J/(kg·°C). The thermal diffusivity of the TIM measured by the xenon flash instrument is 35 mm²/s. The in-plane thermal conductivity of the BN-indium composite-based TIM is around 60 W/mK.

The through-plane thermal conductivity of the BN fiber-indium composite is calculated using Lee's methodology too [81]. Four BN fibers-indium composites with different thicknesses are sandwiched between two copper plates ($8 \times 8 \text{ mm}^2$, 1 mm in thickness) by reflow ($180 \text{ }^\circ\text{C}$, 80 s) at 200 kPa pressure, respectively. As seen in Figure 4.4, there is a linear correlation between bondline thickness (d) and total thermal resistance (R_{Total}). By extrapolation, the interfacial contact resistance $2R_{\text{contact}}$ between Cu and TIM is found to be $0.4 \text{ K}\cdot\text{mm}^2/\text{W}$, i.e. $0.2 \text{ K}\cdot\text{mm}^2/\text{W}$ per interface. The thermal conductivity of the BN fiber-indium composite is found as the reciprocal slope of the line in Figure 4.4, giving a value of 20 W/mK ($1/0.0507$). This is one third of the in-plane thermal conductivity because of the anisotropy of hBN materials. The thermal conductivity of hBN in a parallel direction to the (002) plane is one order of magnitude higher than that perpendicular to the base plane. The BN fibers are parallel to the (002) plane, which is also the in-plane direction of the composite film.

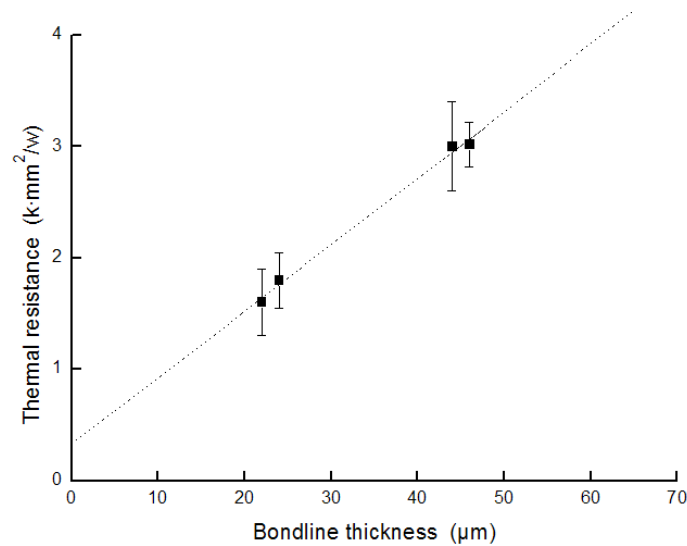


Figure 4.4: Total thermal resistance of BN fibers-indium composite sandwiched between two copper plates at various bondline thicknesses.

4.2 Carbon fiber-SnAgCu composite-based TIM

4.2.1 Composite fabrication

Carbon based materials, such as carbon fibers (CFs), carbon nano-fibers (CNFs), carbon nanotubes and graphene are attractive materials for thermal management applications due to their outstanding thermal and mechanical properties [28, 41-44, 113]. Owing to the unique polynuclear ring structure, mesophase pitch can self-organize to form highly organized crystalline carbon structures at high temperature annealing. This makes mesophase pitch a promising alternative to polyacrylonitrile (PAN) in the development of advanced carbon-based engineering composite materials [114, 115]. Thermally conductive materials based on pitch materials have been reported by several groups as an aligned graphitic foam [115], micro-sized carbon fibers [116] and graphitic blocks [117]. The measured thermal conductivity of different pitch based materials ranges from tens to hundreds W/mK . High thermal properties are expected from the new composite made from carbon fiber and solder matrix.

Mesophase pitch is obtained from the Mitsubishi chemical company, Japan. The mesophase pitch is an aromatic compound and has a softening point of 275 to $295 \text{ }^\circ\text{C}$. A homogeneous

pitch and PI mixture is prepared by dispersing pitch and polyimide powder in a DMAC solvent and stirred for 24h at room temperature. For the electrospinning, a voltage of 18 kV is applied to the cannula and the solution is fed at a rate of 2 ml/h. The samples obtained from the electrospinning are pre-heated in an air atmosphere to 310 °C for 20 min at a 1 °C/min heating rate. After of stabilization, the fiber mat is then carbonized under N₂ at 1000 °C for 2 h with a heating rate of 1 °C/min using a quartz tube furnace. The carbon fiber film is infiltrated by the pressure assisted liquid infiltration and the process mentioned before.

The resultant carbon fibers have diameters in the range of 1-2 micron with a uniform size distribution (Figures 4.5a, b and c). However, the carbonization treatment caused the fiber mats and individual fibers to shrink (Figure 4.5c). TEM study of the carbon fibers indicates that the fiber has a disordered arrangement due to the low carbonization temperature at 1000 °C.

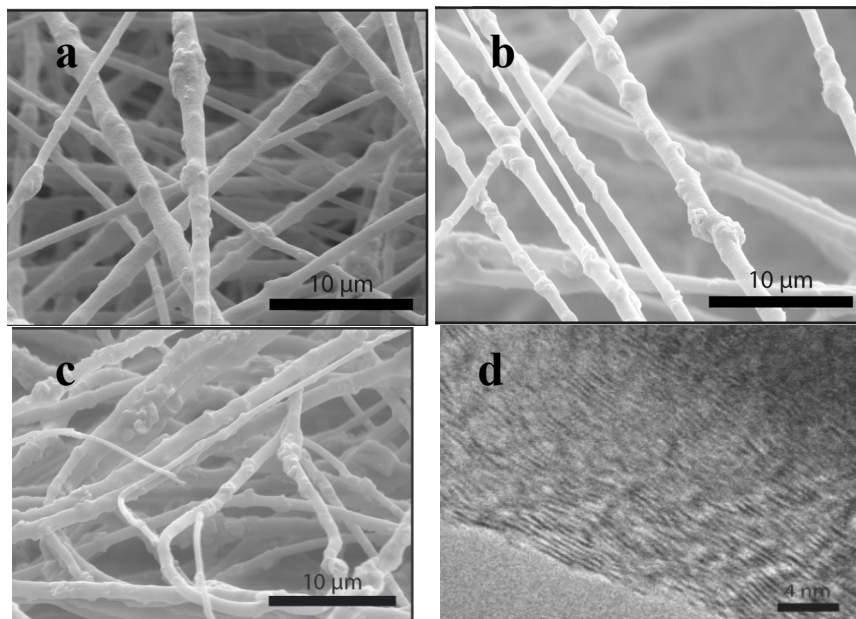


Figure 4.5: SEM images of electrospun pitch-PI fiber (a), stabilized pitch-PI fiber (b), carbon fiber obtained from carbonization at 1000 °C (c), and TEM image of the final carbon fiber.

4.2.2 Characterization of thermal performance

The in-plane thermal conductivity of the carbon fiber-SnAgCu composite is found to be 41 W/mK. The effective through-plane thermal conductivity for carbon fiber-SnAgCu composite is found to be 20 W/mK over the range of 50 to 90°C at 65μm thickness, and the results are summarized in Figure 4.6. The total thermal interface resistance of the sandwich-structure as shown in the Figure 4.6e is measured to be 2-7 Kmm²/W.

To assess the reliability of the carbon fiber-SnAgCu composite for joint performance, thermal cycling of the test assemblies is carried out. The temperature is cycled between -40 to 115°C. Figure 4.6d shows that the thermal resistances remain largely unaffected after 1000 cycles, indicating that a reliable joint has been formed. The observable trend of an increases in thermal resistance of a few percent is within the accuracy of the measurements.

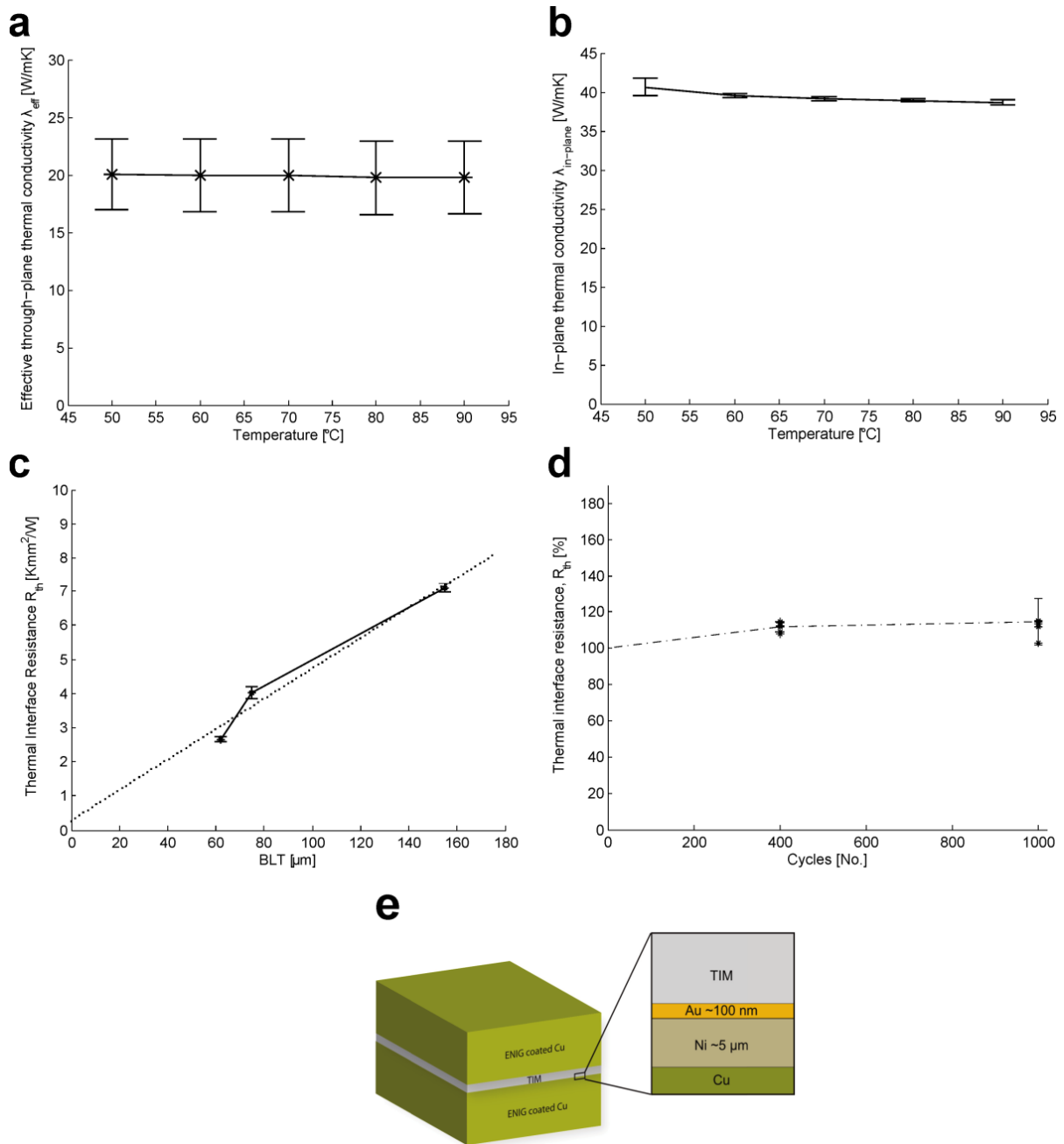


Figure 4.6: Effective through-plane thermal conductivity of carbon fiber-SnAgCu composite between 50 to 90 °C (a), in-plane thermal conductivity of carbon fiber-SnAgCu composite (b), total thermal interface resistance of carbon fiber-SnAgCu composite at various thicknesses (c), relative change in thermal resistance of carbon fiber-SnAgCu composite after thermal cycling up to 1000 cycles (d) and the schematic of carbon fiber-SnAgCu composite test structure used in all the through-plane thermal conductivity measurements and thermal cycling (e).

4.3 Summary and Discussion

BN fiber-indium composite-based TIMs have been fabricated and characterized. The nano-fibrous BN structure is fabricated by electrospinning, heat treatment and Ti/Au coating,

then subsequently being infiltrated with indium. The BN fiber network defines the geometry of the composite and contributes to the heat dissipation in the in-plane direction. The indium phase provides the binding and high thermal conductivity through the continuous metal path in through-plane. Measurements by a xenon flash apparatus show the in-plane thermal conductivity of the composite to be 60 W/mK and the through-plane thermal conductivity to be 20 W/mK, with a thermal contact resistance (R_{contact}) of 0.2 K·mm²/W. However, the presentation of turbostratic structure influences the thermal conduction because of the disordered atom arrangement [96, 97, 118]. Therefore, it is promising to improve the thermal performance of the BN fibers-indium composite-based TIMs by higher temperature annealing to achieve completely hexagonal structure. The strength of the BN fibers could also increase with the higher degree of crystallinity. Another optimization is to employ chemical surface modification to replace the sputtering method to get better wetting with the metal matrix.

In addition, carbon fiber-SnAgCu composites with an anisotropic thermal conductivity of 41 W/mK and 20 W/mK in-plane and through-plane are developed. The carbon fiber is obtained from mesophase pitch that is electrospun with PI and annealed at 1000 °C. The carbon fiber films are highly flexible and easy to handle. Assembled as an interface material, in a test structure, the carbon fiber-SnAgCu composite shows low total thermal interface resistances in the range of 2-7 Kmm²/W. Measurements after 1000 temperature cycles indicate high reliability, as no increase in thermal interface resistance is detected. Consequently, the developed carbon fiber based composite can be suitable for implementation as a TIM for the thermal management of microelectronics.

Chapter 5

Conclusions and outlook

This thesis emphasizes the characterization of metal based materials for interconnect and thermal dissipation applications in electronics packaging. These materials are applied in complicated integrations operating under electrical, thermal and mechanical loading conditions. The nano-scale oxide of lead-free solder particles is analyzed in the first section of the thesis. The consecutive section focuses on the studies of the thermal performance and mechanical properties of novel fiber network metal matrix composite-based TIM.

The precise measurement of the nano-scale oxide layer on the surface of lead-free solder particles is of importance to the quality of the solder joint and the reliability of the packaged system. Using the FIB technology, TEM samples of micro-scale solder particles are prepared without destroying the nano-scale oxide layer. According to the TEM results, an intersection analysis of the AES profile is developed to measure the thickness of surface oxide of solder powders. Using the intersection analysis, it is found that the surface oxide thickness is proportional to the square root of the oxidation time. The FIB-TEM technique and AES intersection analysis with nano-resolution are significant for the oxide control issues, e.g. the Sn based solder in microelectronics packaging or the SnO₂ gas sensor. The intersection analysis method is also recommendable for other oxide studies referring to AES depth analysis.

The second concern of this thesis focuses on the urgent need for novel TIMs with improved thermal performance and mechanical properties. In response to the critical needs in the current thermal management of electronics packaging, we focus on the TIMs with a pragmatic design, which are required to provide high thermal transfer efficiency, low weight, acceptable material and fabrication costs, especially assembly compatibility with the soldering process. Five kinds of fiber network and metal matrix composite-based TIMs have been developed. The novel

fiber-metal matrix composite consists of 3D porous electrospun continuous polyimide fibers and infiltrated solder matrix.

The polymer fiber metal matrix composite-based TIMs have been examined in thermal conductivity tests. The infiltrated metal matrix is decisive for the composite's thermal dissipation ability. The introduction of the fiber network makes the composite thermally anisotropic. The polymer fiber-metal matrix interface of the composite is crucial for the thermal performance. It is found that the solid bonding between the fiber and indium or SnAgCu is presented via the formation of a nanoscale AgIn₂ IMC layer. With the formation of the nano-scale IMC layer, the inner contact resistance of the composite is limited to a very low level. Besides the conventional thermal testing, the polymer fiber-indium composite-based TIMs are also studied for the heat dissipation effect by a chip-TIM-heat spreader testing system with various packaging sizes: 5×5, 10×10, 20×20 and 30×30 mm². The steady-state junction temperature and thermal resistance of the polymer fiber-indium composite are superior to those of current commercial thermal grease. The composite's deformation behaviors are also evaluated. The shear strengths of the TIM with different pressures, mating surfaces and holding times in thermal-humidity conditions are detected. In addition, the polymer fiber-indium composite exhibits the ultimate tensile strength five times higher than that of pure indium, and the strength of the composite exceeds the summation of strengths of its individual components. With rising temperature, the tensile strength decreases while the elongation at fracture increases. Tensile cracks propagate along the fiber-indium interfaces and the arrangement of fibers changes the direction of crack growth. The ultimate tensile strength of the composite is found to be inversely proportional to the logarithmic strain rate in a certain range. In-situ TEM straining of the composite shows the tensile crack initiates from indium and propagates to the fiber-indium interface, and then continues to grow after breakage of the fiber. The obstacle effects from GB and fiber-indium interfaces strengthen the composite by forming solid mutually reinforcing structures. The strengthening mechanism highlights the compression at the fiber-indium interfaces, and then the resultant high bonding strength at the interfaces improves the resistance of relative motion of fiber and indium. As a result of these effects, the tensile strength and creep resistance of the composite have been improved.

The other developed TIMs are based on the BN fibers and carbon fibers. By electrospinning, the nano-scale BN fibers could be fabricated in volume production and the thickness of the BN fibers film could be easily controlled by spinning time. Measurements by the xenon flash thermal analyzer exhibit 60 W/mK in-plane thermal conductivity and 20 W/mK through-plane thermal conductivity. Although showing better thermal performance to current commercial TIMs, the new materials could be improved further via the heat treatment at a higher temperature and optimized surface modification for BN fibers. Carbon fiber-SnAgCu composite also exhibits high thermal conductivity in-plane and through-plane, and good reliability. BN or carbon fiber needs heat treatment at high temperatures above 2000 °C to obtain graphite-like structure.

Besides the two thermally conductive materials tested, other materials like silicon carbide (over 400 W/mK high-purity single crystals), aluminum nitride are interesting to fabricate in the form of fibers according to our composite design. In additional, the fiber network could be also updated with the commercial pitch-based, vapor-grown carbon fibers with higher thermal conductivities (perhaps approaching 2000 W/mK), or diamond-coated carbon fibers. Furthermore, polymer fiber or the fibers mentioned above could be mixed with high thermally conductive reinforcements, for instance, the diamond, cubic boron nitride particle or carbon nanotubes, fullerene, graphene flakes. In those applications, the reinforcement

coatings to promote adhesion, controlled reinforcement-matrix reactions, and lower contact thermal resistance are the key points to guarantee the thermal performance of the composite. Advanced metal matrix composites are still far from wide using due to the limit of thermo-physical property, manufacturing process, reflow technique and cost. Fundamental research on the improvement of wettability, controlling of interfacial structure and thermal conduction mechanism is of vital importance. Continued improvements should be focused on packaging designs and processes, as well as specific stiffness (the ratio of stiffness and density), outstanding fatigue resistance, excellent corrosion resistance and low CTEs (some nearly zero or near to that of silicon).

Acknowledgements

I am grateful to my supervisor, Prof. Johan Liu, for his advice, encouragement, tolerance and financial support. His effort and help have been invaluable in the preparation of this dissertation and my study, and will forever be remembered. Second, I would like to thank my co-supervisors Dr. Lilei Ye and Dr. Murali Murugesan for their guidance and persistent focus on my project.

I am thankful for all my former and present colleagues in the BioNano System lab: Cristina Andersson, Kjell Jeppson, Teng Wang, Björn Carlberg, Xia Zhang, Yifeng Fu, Zhili Hu, Si Chen, Carl Zandén, Di Jiang, Yong Zhang, Wei Mu, Nan Wang, Shuangxi Sun, Yan Zhang, Xiuzhen Lu and Pengtu Zhang for their friendship, support, discussion and collaboration.

Many thanks go to all of the staff at the Nanofabrication Laboratory in MC2. Special thanks go to Ulf Södervall, Henrik Frederiksen, Christer Andersson and Göran Petersson for their help on various fabrication processes.

Most importantly, my deepest appreciation goes to my wife Lulu Shi and my parents, to whom this dissertation is dedicated.

Bibliography

1. Willis B: **Fundamentals of Microsystems Packaging**. *Soldering & Surface Mount Technology* 2003, **15**(1):60-60.
2. Bailey C, Liu J: **Advanced Manufacturing Process, Lead Free Interconnect Materials and Reliability Modeling for Electronics Packaging**. Bradford, GBR: Emerald Group Publishing Ltd; 2006.
3. Liu J, Salmela O, Särkkä J, Morris J, Tegehall P-E, Andersson C: **Introduction to Reliability and Its Importance**. In: *Reliability of Microtechnology*. Springer New York; 2011: 1-2.
4. Carlberg B: **Integration of Nanofibrous Materials in Microsystem Applications**. PhD thesis, Chalmers University of technology; 2012.
5. Sun P: **Low Cycle Fatigue Reliability and Interfacial Reaction of Lead-free Solder Joints for Electronic Packaging**: PhD thesis, Chalmers University of technology; 2005.
6. Parliament E: **Directive 2002/95/EC on the restriction of the use of certain hazardous substances in electrical and electronic equipment**. 2002:L37/19–L37/23.
7. Parliament E: **RoHS. Official J Eur Union**. 2003.
8. Pang J: **Introduction**. In: *Lead Free Solder*. Springer New York; 2012: 1-5.
9. Loomans ME, Fine ME: **Tin-silver-copper eutectic temperature and composition**. *Metall and Mat Trans A* 2000, **31**(4):1155-1162.
10. Johan L, Andersson C, Yulai G, Qijie Z: **Recent Development of Nano-solder Paste for Electronics Interconnect Applications**. In: *Electronics Packaging Technology Conference, 2008 EPTC, 9-12 Dec. 2008*: 84-93.
11. NEMI: **National Electronics Manufacturers Initiative**. (<http://www.nemi.org>).
12. Chiu T-C, Lin K-L: **The growth of Sn whiskers with dislocation inclusion upon electromigration through a Cu/Sn_{3.5}Ag/Au solder joint**. *Scripta Materialia* 2009, **60**(12):1121-1124.
13. Lee LM, Haliman H, Mohamad AA: **Interfacial reaction of a Sn-3.0Ag-0.5Cu thin film during solder reflow**. *Soldering & Surface Mount Technology* 2013, **25**(1):15-23.
14. Zeng K, Tu KN: **Six cases of reliability study of Pb-free solder joints in electronic packaging technology**. *Materials Science and Engineering: R: Reports* 2002, **38**(2):55-105.
15. Görlich J, Oberdorfer C, Baither D, Schmitz G, Reinke C, Wilke U: **The role of oxide layers in solder joints**. *Journal of Alloys and Compounds* 2010, **490**(1–2):336-341.
16. Hung F-Y, Lin H-M, Chen P-S, Lui T-S, Chen L-H: **A study of the thin film on the surface of Sn–3.5Ag/Sn–3.5Ag–2.0Cu lead-free alloy**. *Journal of Alloys and Compounds* 2006, **415**(1–2):85-92.
17. Kuhmann J, Preuss A, Adolphi R, Maly K, Wirth T, Oesterle W, Pittroff W, Weyer G, Fanciulli M: **Oxidation and reduction kinetics of eutectic SnPb, InSn and AuSn: a knowledge base for fluxless solder bonding applications**. In: *Electronic Components and Technology Conference, 1997 Proceedings, 47th: 18-21 May 1997*: 120-126.
18. Luo X, Du W, Lu X, Yamaguchi T, Jackson G, Ye LI, Liu J: **Surface oxide analysis of lead-free solder particles**. *Soldering & Surface Mount Technology* 2013, **25**(1):39-44.
19. Zhang S, Zhang Y, Wang H: **Effect of oxide thickness of solder powders on the coalescence of SnAgCu lead-free solder pastes**. *Journal of Alloys and Compounds* 2009, **487**(1–2):682-686.
20. Batzill M, Diebold U: **The surface and materials science of tin oxide**. *Progress in Surface Science* 2005, **79**(2–4):47-154.

21. ITRS: **International Technology Roadmap for Semiconductors 2007 Edition - Assembly and Packaging**. 2007.
22. Mahajan R, Chia-pin C, Chrysler G: **Cooling a Microprocessor Chip**. *Proceedings of the IEEE* 2006, **94**(8):1476-1486.
23. ITRS: **International Technology Roadmap for Semiconductors 2013 Edition - IRC Overview**. 2013.
24. Prasher R: **Thermal Interface Materials: Historical Perspective, Status, and Future Directions**. *Proceedings of the IEEE* 2006, **94**(8):1571-1586.
25. Latham Carol A MMF: **Thermally conductive ceramic/polymer composites**. *The Carborudum* April 1991: **US 5011872**
26. Bunyan MH: **Double-side thermally conductive adhesive tape for plastic-packaged electronic components**. *Parker-Hannifin* Aug, **13** 2002: **US 6432497**.
27. Chung DDL: **Thermal interface materials**. *Journal of Materials Engineering and Performance* 2001, **10**(1):56-56.
28. Yu A, Ramesh P, Itkis ME, Bekyarova E, Haddon RC: **Graphite Nanoplatelet-Epoxy Composite Thermal Interface Materials**. *The Journal of Physical Chemistry C* 2007, **111**(21):7565-7569.
29. Zhang Y, Xiao A, McVey J: **Advanced Thermal Interface Materials**. *MRS Online Proceedings Library* 2006, **968**.
30. Chen CI, Ni CY, Chang CM, Liu DS, Pan HY, Yuan TD: **THERMAL CHARACTERIZATION OF THERMAL INTERFACE MATERIALS**. *Experimental Techniques* 2008, **32**(3):48-52.
31. Due J, Robinson AJ: **Reliability of thermal interface materials: A review**. *Applied Thermal Engineering* 2013, **50**(1):455-463.
32. Fullem TZ, Cotts EJ: **Thermal Conductivity of Thermal Interface Materials**. *MRS Online Proceedings Library* 2007, **1053**.
33. McNamara AJ, Joshi Y, Zhang ZM: **Characterization of nanostructured thermal interface materials – A review**. *International Journal of Thermal Sciences* 2012, **62**(0):2-11.
34. Fujihara T, Cho H-B, Nakayama T, Suzuki T, Jiang W, Suematsu H, Kim HD, Niihara K: **Field-Induced Orientation of Hexagonal Boron Nitride Nanosheets Using Microscopic Mold for Thermal Interface Materials**. *Journal of the American Ceramic Society* 2012, **95**(1):369-373.
35. Sato K, Horibe H, Shirai T, Hotta Y, Nakano H, Nagai H, Mitsuishi K, Watari K: **Thermally conductive composite films of hexagonal boron nitride and polyimide with affinity-enhanced interfaces**. *Journal of Materials Chemistry* 2010, **20**(14):2749-2752.
36. LIU Z, CHUNG, L. DD: **Boron nitride particle filled paraffin wax as a phase-change thermal interface material**, vol. 128. NY, ETATS-UNIS: American Society of Mechanical Engineers; 2006.
37. Lin C, Chung DDL: **Nanostructured fumed metal oxides for thermal interface pastes**. *Journal of Materials Science* 2007, **42**(22):9245-9255.
38. Sim LC, Ramanan SR, Ismail H, Seetharamu KN, Goh TJ: **Thermal characterization of Al₂O₃ and ZnO reinforced silicone rubber as thermal pads for heat dissipation purposes**. *Thermochimica Acta* 2005, **430**(1–2):155-165.
39. Yu H, Li L, Kido T, Xi G, Xu G, Guo F: **Thermal and insulating properties of epoxy/aluminum nitride composites used for thermal interface material**. *Journal of Applied Polymer Science* 2012, **124**(1):669-677.
40. Xu J, Munari A, Dalton E, Mathewson A, Razeeb KM: **Silver nanowire array-polymer composite as thermal interface material**. *Journal of Applied Physics* 2009, **106**(12):124310.
41. Leong C-K, Aoyagi Y, Chung DDL: **Carbon black pastes as coatings for improving thermal gap-filling materials**. *Carbon* 2006, **44**(3):435-440.

42. Fu Y, Qin Y, Wang T, Chen S, Liu J: **Ultrafast Transfer of Metal-Enhanced Carbon Nanotubes at Low Temperature for Large-Scale Electronics Assembly.** *Advanced Materials* 2010, **22**(44):5039-5042.
43. Ghosh S, Subrina S, Goyal V, Nika DL, Pokatilov EP, Balandin AA: **Extraordinary thermal conductivity of graphene: Possibility of thermal management applications.** In: *Thermal and Thermomechanical Phenomena in Electronic Systems (ITherm), 12th IEEE Intersociety Conference on: 2-5 June 2010:* 1-5.
44. Shahil KMF, Balandin AA: **Graphene-based thermal interface materials.** In: *Nanotechnology (IEEE-NANO), 11th IEEE Conference on: 15-18 Aug. 2011:* 1193-1196.
45. Mason LR, Reynolds AB: **Standardization of oxidation induction time testing used in life assessment of polymeric electric cables.** *Journal of Applied Polymer Science* 1997, **66**(9):1691-1702.
46. Salt FW, Thomas JGN: **Determination of the Oxide Film Thickness on Tin.** *Nature* 1956, **178**(4530):434-435.
47. Gabe DR: **Mixed oxide films on tin.** *Surface Technology* 1977, **5**(6):463-478.
48. Preuss A, Adolphi B, Drescher K: **Oxidation of In-48Sn.** *Journal of The Electrochemical Society* 1994, **141**(10):2784-2788.
49. Wang H, Teeter G, Turner J: **Investigation of a Duplex Stainless Steel as Polymer Electrolyte Membrane Fuel Cell Bipolar Plate Material.** *Journal of The Electrochemical Society* 2005, **152**(3):B99-B104.
50. Yuan DW, Yan RF, Simkovich G: **Rapid oxidation of liquid tin and its alloys at 600 to 800°C.** *Journal of Materials Science* 1999, **34**(12):2911-2920.
51. Hart RK: **The Thermal Oxidation of Tin.** *Proceedings of the Physical Society Section B* 1952, **65**(12):955.
52. DIEGUEZ A, ROMANO J, P. N, L. S, G. S: **Analysis of the thermal oxidation of tin droplets and its implications on gas sensor stability,** vol. 146. Pennington, NJ, ETATS-UNIS: Electrochemical Society; 1999.
53. http://www.springermaterials.com/docs/info/10542753_2319.html.
54. Howie A: **Image Contrast And Localized Signal Selection Techniques.** *Journal of Microscopy* 1979, **117**(1):11-23.
55. Pennycook SJ, Nellist PD: **Z-Contrast Scanning Transmission Electron Microscopy.** In: *Impact of Electron and Scanning Probe Microscopy on Materials Research.* Edited by Rickerby D, Valdrè G, Valdrè U, vol. 364: Springer Netherlands; 1999: 161-207.
56. <http://micromagazine.fabtech.org/archive/04/07/tracy.html>.
57. Gunawardane R, Arumainayagam C: **AUGER ELECTRON SPECTROSCOPY.** In: *Handbook of Applied Solid State Spectroscopy.* Edited by Vij DR: Springer US; 2006: 451-483.
58. Auger P: **Sur l'effet photoélectrique composé.** *J Phys Radium* 1925, **6**(6):205-208.
59. Atkinson A: **Transport processes during the growth of oxide films at elevated temperature.** *Reviews of Modern Physics* 1985, **57**(2):437-470.
60. Young EWA, Gerretsen JH, de Wit JHW: **The Oxygen Partial Pressure Dependence of the Defect Structure of Chromium(III)Oxide.** *Journal of The Electrochemical Society* 1987, **134**(9):2257-2260.
61. Chiu C-P, Maveety JG, Tran QA: **Characterization of solder interfaces using laser flash metrology.** *Microelectronics Reliability* 2002, **42**(1):93-100.
62. Pritchard LS, Acarnley PP, Johnson CM: **Effective thermal conductivity of porous solder layers.** *Components and Packaging Technologies, IEEE Transactions on* 2004, **27**(2):259-267.
63. Jagannadham K: **Thermal Conductivity of Indium–Graphene and Indium-Gallium–Graphene Composites.** *Journal of Elec Materi* 2011, **40**(1):25-34.

64. Yuquan L, Johnson RW, Zhang R, Henson P, Thompson P, Hooghan T, Libres J: **Ti/Au Die Backside Metallization for Flip Chip Heat Spreader Attachment**. *Electronics Packaging Manufacturing, IEEE Transactions on* 2010, **33**(1):44-54.
65. Too SS, Touzelbaev M, Khan M, Master R, Diep J, Kee-Hean K: **Indium thermal interface material development for microprocessors**. In: *Semiconductor Thermal Measurement and Management Symposium, 25th Annual IEEE: 15-19 March 2009*: 186-192.
66. Deppisch C, Fitzgerald T, Raman A, Fay H, Charles Z, Pilin L, Mikel M: **The Material Optimization and Reliability Characterization of an Indium-Solder Thermal Interface Material for CPU Packaging**. *JOM* 2006, **58**(6):67-74.
67. Hengyun Z, Mui YC, Poh-Eng T, Soon-Hwa N: **Thermal Characterizations of Solid Thermal Interface Materials**. In: *Electronics Packaging Technology Conference, EPTC 10th: 9-12 Dec. 2008*: 1472-1478.
68. Plötner M, Donat B, Benke A: **Deformation properties of indium-based solders at 294 and 77 K**. *Cryogenics* 1991, **31**(3):159-162.
69. Reed RP, McCowan CN, Walsh RP, Delgado LA, McColskey JD: **Tensile strength and ductility of indium**. *Materials Science and Engineering: A* 1988, **102**(2):227-236.
70. Dutta I, Raj R, Kumar P, Chen T, Nagaraj CM, Liu J, Renavikar M, Wakharkar V: **Liquid Phase Sintered Solders with Indium as Minority Phase for Next Generation Thermal Interface Material Applications**. *Journal of Elec Materi* 2009, **38**(12):2735-2745.
71. Goldstein JLF, Morris JW: **Microstructural development of eutectic Bi-Sn and eutectic In-Sn during high temperature deformation**. *Journal of Elec Materi* 1994, **23**(5):477-486.
72. Björn C, Teng W, Johan L, Dongkai S: **Polymer-metal nano-composite films for thermal management**. *Microelectronics International* 2009, **26**(2):28-36.
73. Björn C, Li-Lei Y, Johan L: **Polymer-metal nanofibrous composite for thermal management of microsystems**. *Materials Letters* 2012, **75**(0):229-232.
74. Montesano J, Fawaz Z, Poon C, Behdinin K: **A microscopic investigation of failure mechanisms in a triaxially braided polyimide composite at room and elevated temperatures**. *Materials & Design* 2014, **53**(0):1026-1036.
75. Wang Q, Zhang X, Pei X: **Study on the synergistic effect of carbon fiber and graphite and nanoparticle on the friction and wear behavior of polyimide composites**. *Materials & Design* 2010, **31**(8):3761-3768.
76. Chen B, Wang J, Yan F: **Synergism of carbon fiber and polyimide in polytetrafluoroethylene-based composites: Friction and wear behavior under sea water lubrication**. *Materials & Design* 2012, **36**(0):366-371.
77. Sroog CE: **Polyimides**. *Progress in Polymer Science* 1991, **16**(4):561-694.
78. Chen F, Peng X, Li T, Chen S, Wu X-F, Reneker DH, Hou H: **Mechanical characterization of single high-strength electrospun polyimide nanofibres**. *Journal of Physics D: Applied Physics* 2008, **41**(2):025308.
79. Simić V, Marinković Ž: **Room temperature interactions in Ag-metals thin film couples**. *Thin Solid Films* 1979, **61**(2):149-160.
80. Parker WJ, Jenkins RJ, Butler CP, Abbott GL: **Flash Method of Determining Thermal Diffusivity, Heat Capacity, and Thermal Conductivity**. *Journal of Applied Physics* 1961, **32**(9):1679-1684.
81. Lee TYR: **Thermal Diffusivity of Dispersed and Layered Composites**. PhD thesis, Purdue University; 1977.
82. **GB/T 2423.3-2001: Environmental testing for electric and electronic products: Test methods-Test Cb: Damp heat, steady state, primarily for equipment**.
83. Chen D, Wang R, Tjiu WW, Liu T: **High performance polyimide composite films prepared by homogeneity reinforcement of electrospun nanofibers**. *Composites Science and Technology* 2011, **71**(13):1556-1562.

84. Ishiyama A, Sasaki M, Susa T, Kim SB, Tsuda M, Yumura H, Ohmatsu K, Sato K, Kim S, Ledbetter H: **Low-temperature elastic coefficients of polycrystalline indium.** *Materials Science and Engineering: A* 1998, **252**(1):139-143.
85. R. V. Safiullin, Vasin RA, Enikeev FU: **DETERMINATION OF THE PARAMETERS OF SUPERPLASTIC FORMING FOR LONG RECTANGULAR THIN SHEET TITANIUM ALLOY Ti-6Al-4V.** *Acta Metallurgica Sinica* 2000, **13**(2):567-573.
86. Abrahams MS, Liebmann WK: **The dependence of the tensile behavior of insb on temperature, strain-rate and oxygen content.** *Acta Metallurgica* 1962, **10**(10):941-949.
87. Van Der Biest O, Van Der Planken J: **The plastic deformation of indium single crystals.** *Acta Metallurgica* 1973, **21**(12):1629-1639.
88. Blind JM, George A, Champier G: **Dislocations and Slip Systems in Indium Single Crystals.** In: *Strength of Metals and Alloys.* Edited by Haasen P, Gerold V, Kostorz G: Pergamon; 1979: 175-179.
89. Gerberich W, Jungk JM, Mook WM: **8.10 - Crack–Dislocation Interactions.** In: *Comprehensive Structural Integrity.* Edited by Milne I, Ritchie RO, Karihaloo B. Oxford: Pergamon; 2003: 357-381.
90. Kumar J, Srivastava ON: **The Electron Microscopic Observation of Mechanical Twins in Gadolinium.** *physica status solidi (b)* 1969, **32**(1):391-397.
91. Ochiai S, Osamura K: **Tensile strength of fibre-reinforced metal matrix composites with non-uniform fibre spacing.** *Journal of Materials Science* 1989, **24**(10):3536-3540.
92. Markaki AE, Clyne TW: **Magneto-mechanical actuation of bonded ferromagnetic fibre arrays.** *Acta Materialia* 2005, **53**(3):877-889.
93. Tsarouchas D, Markaki AE: **Extraction of fibre network architecture by X-ray tomography and prediction of elastic properties using an affine analytical model.** *Acta Materialia* 2011, **59**(18):6989-7002.
94. Haubner R, Wilhelm M, Weissenbacher R, Lux B: **Boron Nitrides — Properties, Synthesis and Applications.** In: *High Performance Non-Oxide Ceramics II.* Edited by Jansen M, vol. 102: Springer Berlin Heidelberg; 2002: 1-45.
95. Patnaik P: **Handbook of inorganic chemicals.** NewYork, United States: McGraw-Hill. 2003.
96. Kelly BT: **The thermal conductivity of hexagonal boron nitride parallel to the basal planes.** *Journal of Nuclear Materials* 1977, **68**(1):9-12.
97. Sichel EK, Miller RE, Abrahams MS, Buiocchi CJ: **Heat capacity and thermal conductivity of hexagonal pyrolytic boron nitride.** *Physical Review B* 1976, **13**(10):4607-4611.
98. Paine RT, Narula CK: **Synthetic routes to boron nitride.** *Chemical Reviews* 1990, **90**(1):73-91.
99. Ziyin L, Yagang Y, McNamara A, Kyoung-sik M, Wong CP: **Single/few-layer boron nitride-based nanocomposites for high thermal conductivity underfills.** In: *Electronic Components and Technology Conference (ECTC), IEEE 62nd: May 29 2012-June 1 2012:* 1437-1441.
100. Song W-L, Wang P, Cao L, Anderson A, Meziani MJ, Farr AJ, Sun Y-P: **Polymer/Boron Nitride Nanocomposite Materials for Superior Thermal Transport Performance.** *Angewandte Chemie International Edition* 2012, **51**(26):6498-6501.
101. Economy J, Anderson RV: **Properties and Uses of Boron Nitride Fibers.** *Textile Research Journal* 1966, **36**(11):994-1003.
102. Economy J, Anderson R: **A New Route to Boron Nitride.** *Inorganic Chemistry* 1966, **5**(6):989-992.
103. Lindquist DA, Janik JF, Datye AK, Paine RT, Rothman JB: **Boron nitride fibers processed from poly(borazinylamine) solutions.** *Chemistry of Materials* 1992, **4**(1):17-19.
104. Kimura Y, Kubo Y, Hayashi N: **High-performance boron-nitride fibers from poly(borazine) preceramics.** *Composites Science and Technology* 1994, **51**(2):173-179.

105. Wideman T, Sneddon LG: **Dipentylamine-Modified Polyborazylene: A New, Melt-Spinnable Polymeric Precursor to Boron Nitride Ceramic Fibers.** *Chemistry of Materials* 1996, **8**(1):3-5.
106. Qiu Y, Yu J, Rafique J, Yin J, Bai X, Wang E: **Large-Scale Production of Aligned Long Boron Nitride Nanofibers by Multijet/Multicollector Electrospinning.** *The Journal of Physical Chemistry C* 2009, **113**(26):11228-11234.
107. Qiu Y, Yu J, Yin J, Tan C, Zhou X, Bai X, Wang E: **Synthesis of continuous boron nitride nanofibers by solution coating electrospun template fibers.** *Nanotechnology* 2009, **20**(34):345603.
108. Hubáček M, Sato T, Ishii T: **A Coexistence of Boron Nitride and Boric Oxide.** *Journal of Solid State Chemistry* 1994, **109**(2):384-390.
109. Thomas J, Weston NE, O'Connor TE: **Turbostratic Boron Nitride, Thermal Transformation to Ordered-layer-lattice Boron Nitride.** *Journal of the American Chemical Society* 1962, **84**(24):4619-4622.
110. Gladkaya IS, Kremkova GN, Slesarev VN: **Turbostratic boron nitride (BNt) under high pressures and temperatures.** *Journal of the Less Common Metals* 1986, **117**(1-2):241-245.
111. Zedlitz R, Heintze M, Schubert MB: **Properties of amorphous boron nitride thin films.** *Journal of Non-Crystalline Solids* 1996, **198-200, Part 1**(0):403-406.
112. Hamilton EJ, Dolan SE, Mann CM, Colijn HO, McDonald CA, Shore SG: **Preparation of amorphous boron nitride and its conversion to a turbostratic, tubular form.** *Science* 1993, **260**(5108):659-661.
113. Balandin AA: **Thermal properties of graphene and nanostructured carbon materials.** *Nat Mater* 2011, **10**(8):569-581.
114. Qiao WM, Song Y, Hong SH, Lim SY, Yoon SH, Korai Y, Mochida I: **Development of Mesophase Pitch Derived Mesoporous Carbons through a Commercially Nanosized Template.** *Langmuir* 2006, **22**(8):3791-3797.
115. Klett J, Hardy R, Romine E, Walls C, Burchell T: **High-thermal-conductivity, mesophase-pitch-derived carbon foams: effect of precursor on structure and properties.** *Carbon* 2000, **38**(7):953-973.
116. Tzeng S-S, Hung K-H, Ko T-H: **Growth of carbon nanofibers on activated carbon fiber fabrics.** *Carbon* 2006, **44**(5):859-865.
117. Yuan G, Li X, Dong Z, Westwood A, Cui Z, Cong Y, Du H, Kang F: **Graphite blocks with preferred orientation and high thermal conductivity.** *Carbon* 2012, **50**(1):175-182.
118. **Properties of advanced semiconductor materials GaN, AlN, InN, BN, SiC, SiGe.** In: *Scitech Book News*. vol. 25. Portland, United States: Book News, Inc. 2001.